Utrecht University

MSc Climate Physics
Institue for Marine and Atmospheric research Utrecht

Quantifying the historical surface mass balance of the Greenland ice sheet using both RACMO2.4p1 and in situ data, and its correlation with large scale atmospheric circulation

Silvia Del Genovese

Daily supervisor: dr. ir. Maurice van Tiggelen
First supervisor: prof. dr. Michiel R. van den Broeke
Second supervisor: dr. Carleen H. Tijm-Reijmer

Acknowledgements

I wish to thank my supervisors, Michiel and Maurice. I am deeply grateful for the help and guidance you gave me, for the ease of our meetings and the limitless space for questions, doubts, and growth. I want to thank Christiaan for his availability and patience, Carleen, and all the Ice and RACMO people for the fruitful meetings. The time spent on this project was long, and the transition from student to unemployed citizen painful and deep. Yet, I found many friends: fellow students, flatmates, people met by sheer luck; I found people that come from where I come from, people that eventually went where I will never go; people that are just like me. I want to thank you all. Finally, and to me, most importantly, I am grateful to my parents - in a way that's close to guilt, in a way that makes my heart heavy, and dark
you've grown old, and i ve grown up

via via

son passati due anni oramai, quante cose ho imparato lo sai
per un nuovo ricordo, per viverlo addosso
devo perdere un corpo che non avrò mai

son passati due anni, dirai
nuovi sogni, tu non ne ebbi mai
eri sempre a cercare i tuoi passi scordati
le scarpe mangiate dal ieri e domani

ma due anni son come due onde, una ti prende e l'altra ti sputa
e da fresco scroscio non diventi che spuma
dal faro di luce non vedi che bruma

che due anni son come due sponde, se attraversi anche tu questo fiume

ad alcuni la corrente porterà via ad altri una mano terrà compagnia

Abstract

Increase in surface melting is the main contributor to Greenland Ice Sheet (GrIS) mass loss, therefore its quantification is extremely relevant in assessing the future rise of sea levels. However, direct measurements of surface melt and runoff are difficult and present many gaps in time and space. Therefore, numerical modeling is essential to calculate melt and assess the current state of the GrIS Surface Mass Balance (SMB), which is the sum of the mass fluxes removing or accumulating mass at the ice-sheet surface. Besides this, the last decades have been marked by a shift in the atmospheric circulation over Greenland, with more negative North Atlantic Oscillation (NAO) phases and higher frequency blocking events during summer that increased the Greenland Blocking Index (GBI). These accompany the decrease in SMB, bringing relatively warm and moist air towards the GrIS. This study uses the latest output of the Regional Atmospheric Climate Model RACMO2.4p1 (5.5 km horizontal resolution) and observations from selected Automatic Weather Stations (AWSs) and annual stakes measurements to: (1) evaluate the model performance; (2) reconstruct the GrIS integrated Surface Mass Balance (SMB) and its components from 1945 to 2023; (3) relate the interannual variability of SMB and SMB components to GBI variability, highlighting the connections between summer melt and higher GBI values. The results show that (1) RACMO2.4p1 underestimates the net shortwave radiation (-3 W/m^2) due to a delayed onset of the melting season. The SHF is also underestimated (-2 W/m^2), hence leading overall to an underestimation of melt energy, especially in the low-lying stations (i.e. KAN_L, QAS_L, TAS_L), for which the SMB bias between modeled and observed annual SMB is higher (0.1 m w.e. yr^{-1} for stations above 1000 m a.s.l. vs. 1.7 m w.e. yr^{-1} below 1000 m a.s.l.). (2) The modeled GrIS integrated SMB between 1945 and 2023 is 491 Gt yr^{-1}, the integrated runoff is 257 Gt yr^{-1} and the integrated accumulation is 822 Gt yr^{-1}. The rate of integrated SMB decline accelerated from 1982, which marks the onset of a series of climatological periods characterized by the most rapid decreases in SMB. (3) Finally, the SMB is anti-correlated to the summer GBI (R^2=-0.67) through the correlation between summer melt and summer GBI (R^2=0.85). Both

correlations show different spatial sensitivity to GBI, whereas the integrated SMB shows a decrease of 102 Gt/yr when the summer GBI increases by one-standard-deviation. Therefore, this study highlights the important relationship between SMB and summer GBI, and the necessity of realistically simulating regional circulation variability to model future GrIS SMB, as much as refining RACMO2.4p1 to better constrain the current state of the GrIS SMB.

Contents

1 Introduction **6**

2 Methods **8**
2.1 Surface Mass Balance (SMB) and Surface Energy Balance (SEB) 8
2.2 Model Evaluation 10
2.2.1 RACMO2.4p1 10
2.2.2 Model Output 11
2.2.3 Observations 12
2.2.4 RACMO2.4p1 Data Treatment 17
2.3 GrIS Integrated SMB and SMB components 18
2.4 GrIS SMB variability and Summer GBI 19
2.4.1 Atmospheric Circulation over Greenland and the GBI 19
2.4.2 GBI dataset description 21
2.4.3 SMB, SEB and GBI 22

3 Results **23**
3.1 Model evaluation 23
3.1.1 SEB Variables 23
3.1.2 Surface Mass Balance and Melt 26
3.2 Greenland Ice Sheet Integrated SMB 31
3.3 Greenland Blocking Index and Surface Mass Balance 34
3.3.1 SMB, GBI and Melt Connections 34
3.3.2 Spatial correlations 34

4 Discussion **38**
4.1 Model Evaluation 38
4.1.1 SMB 44

4.2 Integrated SMB Variability and GBI Melt connections 46
4.2.1 SMB: annual and spatial variability 46
4.2.2 Connections with GBI 46

Conclusions **49**

Bibliography **51**

Chapter 1

Introduction

The Greenland Ice Sheet (GrIS) plays a pivotal role in the current rise in global sea levels (Shepherd et al., 2020), contributing through various processes that lead to ice mass loss. These processes are primarily categorized as dynamical ice loss and surface meltwater runoff, and since the 1990s, both mechanisms have increased, contributing equally to the mass loss of the GrIS (King et al., 2020). However, surface meltwater runoff has increasingly dominated since 2000, driven by intensified surface melt and a consistent decline in Surface Mass Balance (SMB), which is the net budget of all the mass fluxes that determine surface accumulation and ablation (Fettweis et al., 2017; Hanna et al., 2021; van den Broeke et al., 2016). This acceleration in melt has been linked to shifts in atmospheric circulation over Greenland, particularly the increased frequency of blocking patterns that enhance the advection of warm, moist air, and that can modulate extreme events like heatwaves that further amplify GrIS mass loss (Hanna et al., 2021) . These patterns are quantified through the Greenland Blocking Index (GBI), which provides a measure of atmospheric blocking intensity (Fettweis et al., 2013) based on the mean atmospheric pressure at 500 hPa over Greenland (Hanna, Hall, et al., 2018). Global circulation models (GCMs) struggle to represent the recent negative summer (JJA) NAO phases and higher GBI values (Hanna, Fettweis, and Hall, 2018). Therefore, it is important to understand how the GBI can be better predicted and if it is possible to use summer GBI values as predictor for future annual SMB. To quantify the long-term and present state of the GrIS SMB, in situ observations are not enough due to their discontinuity in both time and space. Therefore, numerical models are widely used since they can fill the space-time observational gaps and give an accurate representation of the whole GrIS mass balance (Fettweis, 2007). For this purpose, limited-area Regional Climate Models are the most used for their higher spatial resolution and dedicated parameterisations, and

in this study SMB and SEB variables simulated by the updated Regional Atmopheric Climate Model (RACMO) in its polar version 2.4p1 (RACMO2.4p1) are presented with the aim of:

1. Evaluating the model using in situ observations from Automatic Weather Stations (AWSs);

2. Use the SMB output to reconstruct the evolution of the integrated GrIS SMB from 1945 to 2023;

3. Find whether there is any correlation between the RACMO2.4p1 SMB variability and atmospheric conditions as quantified by the GBI.

To achieve these objectives, different methods were used, which are explained in the Methods section along with more thorough definitions of basic concepts used in this study (the SMB, the SEB, how the GBI is defined) and of the regional atmospheric model, RACMO2.4p1, of which the output was used. Successively, the Results section illustrates the obtained results showing time-series, bias plots and maps realized from the used methods. The Discussion section explains in more detail how the results are found in the context of the physical processes occurring in Greenland and how they control and relate to the SMB and the GBI. Finally, the Conclusions will answer the research questions and provide suggestions for further studies.

Chapter 2

Methods

This section deals with the methods, providing the basic concepts and processes analyzed in this work. The SMB, its components, the SEB variables and the atmospheric circulation over Greenland with the GBI will be first explained. We use data from the latest version of the Regional Atmospheric Climate model RACMO2.4p1, therefore the model and its evaluation are presented, along with the handling of the data and a description of the observational dataset with which the evaluation was done. We describe how the integrated GrIS SMB and components were computed from RAMCO2.4p1. Finally, the GBI dataset is described and correlated to the SMB/SEB variables from the model.

2.1 Surface Mass Balance (SMB) and Surface Energy Balance (SEB)

The total mass balance (MB) of the grounded GrIS is given by the mass gains at the surface (SMB) minus the mass that is lost through solid ice discharge across the ice sheet grounding line (D) over one year, therefore representing the GrIS integrated fluxes, expressed in Gt year $^{-1}$:

$$MB = \frac{\partial M}{\partial t} = SMB - D \tag{2.1}$$

The SMB can be either positive or negative since it considers all the mass fluxes directed towards and away from the ice sheet surface:

$$SMB = P_{tot} - SU_{tot} - ER_{ds} - RU \tag{2.2}$$

And is specific, with units of kg m^{-2} yr^{-1}. P_{tot} represents the total precipitation (snowfall, SN, plus rainfall, RA), SU_{tot} the total sublimation (at the surface and from the drifting snow), ER_{ds} is the erosion of the snow due to the divergence of the drifting snow transport, and RU is the runoff of meltwater. If the accumulation and ablation terms are not in balance, SMB assumes either a positive or negative sign, partly determining the mass balance of the GrIS. The SMB in (3.2) is more commonly called climatic mass balance and deviates from its formal definition, given that it does not only considers surface processes, but also subsurface processes such as water retention and refreezing. The SMB varies significantly across regions and seasons, with higher accumulation occurring in winter and enhanced melting taking place at lower elevations during summer, even though the SMB is defined over the entire year. The liquid water balance equation explains the runoff term in the SMB equation, and considers all processes that generate or remove liquid water present in the ice column, from the surface down to the firn/ice transition:

$$RU = RA + CO + ME - RT - RF \tag{2.3}$$

Here, runoff (Gt year $^{-1}$) is given as the sum of sources: melt water (ME), rainfall (RA) and condensation (CO), while water retention (RT) and refreezing (RF) are sinks, since they store the melt water in the ice column, reducing runoff. Finally, melt (ME), but also surface sublimation and condensation, are all determined by the Surface Energy Balance (SEB), which is the sum of all the energy fluxes towards and away from the surface:

$$0 = SEB = SW_{net} + LW_{net} + SHF + LHF + GHF - M \tag{2.4}$$

$$M = SW_{net} + LW_{net} + SHF + LHF + GHF \tag{2.5}$$

Where energy fluxes are in Wm^{-2} and are positive when directed towards the surface. SW_{net} is given by $SW_{net} = SW_{in} + SW_{out} = SW_{in}$ (1- α), where α is surface albedo; LW_{net} is dependent on the incoming LW and the surface temperature through the formula $LW_{net} = LW_{in}$-σ T_s where σ is the Stefan Boltzmann's constant ($\sigma = 5.67 \times 10^{-8}$ W m^{-2} K^4), T_s is the temperature of the snow/ice surface (skin temperature) and surface emissivity is assumed to equal one. SHF, LHF and GHF are respectively the sensible, latent and ground heat fluxes. The SHF depends on the vertical gradient of wind speed and temperature, while the LHF is controlled by the vertical gradient of wind speed and specific humidity. The GHF is usually small when studying monthly/yearly fluctuations on average, while significant on subdaily time scales. In this equation no SW radiation is assumed to penetrate below the surface. This way, a value for T_s can be iteratively found for which the SEB equals

zero. If the found T_s value is greater than 0°C, the temperature is reset to 0°C and any excess energy is allocated to melt energy (M). Iteration is needed due to non-linearity and coupled processes within the equation, since the turbulent heat fluxes depend on the value of T_s itself, and the outgoing long-wave radiation flux is non-linearly dependent on skin temperature (van den Broeke et al., 2016; van den Broeke et al., 2017).

2.2 Model Evaluation

2.2.1 RACMO2.4p1

As introduced, numerical models are necessary to overcome the space and time gaps of observations for the SMB of the GrIS and other variables. The main dataset used in this study was the latest output of the updated polar Regional Atmospheric Climate Model, RACMO2.4p1, developed at the Institute for Marine and Atmospheric Research Utrecht (IMAU). The model itself was created at the Royal Netherlands Meteorological Institute (KNMI) in collaboration with the Danish Meteorological Institute (DMI) in the 1990s, after which a polar version (identified with the letter 'p') with specific parameterizations to better simulate polar regions was developed at IMAU. These include a glaciated surface tiles where a multilayer snow model is adopted, to account for complex snow processes like snow metamorphism, compaction, melt and refreezing (van Dalum et al., 2021, 2024). RACMO uses the High Resolution Limited Area Model (HIRLAM) (Undén et al., 2002) to simulate the dynamical processes of the atmosphere. In HIRLAM, a semi-Lagrangian and semi-implicit scheme is employed to track air parcels at the fixed points of the Eulerian grid. Their evolution over time is then computed by using a two-step integration method for the momentum equations. In the first half-step, the Coriolis term is implicitly integrated (to maintain stability), while the pressure gradient term is explicitly integrated. In the second half-step, the process is reversed, with the Coriolis term integrated explicitly and the pressure gradient term implicitly. This approach helps to preserve numerical stability while allowing the use of unconditionally large time steps (Undén et al., 2002). Regarding physical processes, RACMO uses the Integrated Forecasting System (IFS) of the European Center for Medium-Range Weather Forecasts (ECMWF) model. RACMO2.4p1 employs HIRLAM 5.0.3 dynamical core, as its previous version, RACMO2.3p2, but presents major improvements regarding the IFS physics modules, going from cycle 33r1 (ECMWF, 2009) to cycle 47r1 (ECMWF, 2020; van Dalum et al., 2024). Other processes are better represented through specific parameterizations made separately from the new 47r1 IFS cycle.

Some of the most relevant improvements (in terms of ice sheet surface energy and mass balance) regard the water content of clouds, for which now different prognostic variables for liquid water and ice are present, and they can interact in the formation of mixed-phase clouds, so that both clouds and the formation of precipitation are better represented (van Dalum et al., 2024); rain and snowfall are also separate variables and have distinct fall speeds and horizontal advection: instead of being immediately deposited at its formation location, snow can be advected horizontally before accumulating at the ground, which is especially important in regions where strong winds are present, like in southeast Greenland e.g. at the QAS-stations, where observed snowfall is high (Hermann et al., 2018); long-wave radiation scattering within clouds is improved, to increase the accuracy in simulating how clouds trap and emit heat (van Dalum et al., 2024); the ice cover is now fractional (from 10% to 100%), overcoming the binary field for which grid cells were either fully ice covered or ice free, and allowing for a more detailed and realistic representation of how ice interacts with the surface and the atmosphere, especially at lower ablation regions. All these improvements are presented in more detail in van Dalum et al. (2024), along with all the other improvements made in the model not mentioned here.

2.2.2 Model Output

Being a limited-area model, RACMO2.4p1 is forced at its lateral boundaries with 3-hourly ERA5 multilevel reanalysis data (Hersbach et al., 2020) for wind speed, temperature, humidity and pressure from 1940, with a spin-up period of 5 years, and is nudged at its upper boundary (van Dalum et al., 2024). The dataset therefore covers a period that runs from 1945 to 2023, extending further in time than RACMO2.3p2 (1958–2016) and has a spatial resolution of 5.5 km (Noël et al., 2018). The land-ice mask is based on the bed topography and bathymetry map of Greenland from the BedMachine project (BedMachine Greenland 5, Morlighem et al., 2021) and covers Greenland, Iceland, Svalbard and part of Arctic Canada. The variables of interest from the extensive RACMO2.4p1 output for this study were the energy fluxes involved in the Surface Energy Balance (SEB): downward and upward shortwave and longwave radiation, sensible and latent heat fluxes; near-surface meteorology variables: specific humidity, wind speed and air temperature; SMB and SMB components (for glaciated tiles only) melt, runoff, total precipitation and refreezing. As a first step in the model evaluation, time-series of the mentioned variables were extracted at the selected AWSs' locations by selecting the pixels in the model that are closest to the coordinates of the selected AWSs. As a consequence, small mismatches between real vs. modeled AWSs' locations and elevations are present and/or differ-

ent stations are modeled in the same pixel, like S5 and KAN_L or S10 and KAN_U along the K-Transect (in table 2.1 and 2.2). Interpolation between the four closest points as done in other studies (van Dalum et al., 2021) was not chosen here since it introduces a new uncertainty and prevents a direct comparison of the model with observations, which is the main purpose of this research.

2.2.3 Observations

The RACMO2.4p1 model output was compared to observational data from AWSs. The observational dataset used in this study is from PANGEA (Tiggelen et al., 2024) and includes SEB energy fluxes components (daily averages) from 19 Automatic Weather Stations (AWSs) from both PROMICE and IMAU. AWSs started being deployed in Greenland from the 1990s, allowing for year-round measurements and a higher spatial coverage than previous observations. Key programs include the Greenland Climate Network (GC-Net) (Vandecrux et al., 2023) initiated in 1990 and the K-Transect, which started in 1993 in the south-west of Greenland (Smeets et al., 2018). Since then, many other AWS were installed, and in 2007 the Programme for Monitoring of the Greenland Ice Sheet (PROMICE) started. The PROMICE network presently includes 25 AWSs across the Greenland Ice Sheet (GrIS), mainly in the ablation area, to complement the AWSs located in the accumulation regions from the GC-Net programme. PROMICE AWSs are strategically placed at different elevations with a lower (L) station close to the ice margin in the ablation zone and an upper (U) complementary one closer to the equilibrium line (ELA - where mass gains and losses balance) or in the accumulation zone. The studied AWSs are:

1. KAN_L, KAN_M and KAN_U stations, located along the southwestern slope of the GrIS, near Kangerlussuaq, with KAN_U being the highest at 1840 m, close to the accumulation zone, while KAN_L and KAN_M are in the ablation zone;

2. KPC_L, KPC_U: situated in Kronprins Christian Land in northeastern Greenland, with the lower station (KPC_L) near the ice margin and the upper station (KPC_U) higher up at 870 m, near the ELA;

3. QAS_L, QAS_M and QAS_U, QAS_A, located in the Qassimiut region, ranging from the ice margin around 288 m to upper elevations, 1008 m, but still inthe ablation zone. The higher station (QAS_A) only has one year of data, and the 'M' in QAS_M stands for 'middle';

4. TAS_L, TAS_U and TAS_A, in the Tasiilaq region, also spatially spread to monitor varying climatic conditions.

The AWSs from IMAU (Utrecht University) were initiated in the 1990s but started collecting robust data in 2003 with stations S5, S6, S9 near Kangerlussuaq in western Greenland along the K-Transect, to which S10 was successively added in the lower accumulation zone in 2010 (Smeets et al., 2018). In addition to these, also station S21 near the QAS - PROMICE stations and stations S22-S23 were employed in this study, for a total of 7 AWSs from IMAU and 12 from PROMICE. The location and names of the stations are presented in Fig. 2.1 , while their exact coordinates, elevation and activity period are given in table 2.1 and 2.2, where also the modeled latitude, longitude and elevation from RACMO2.4p1 are showed for comparison.

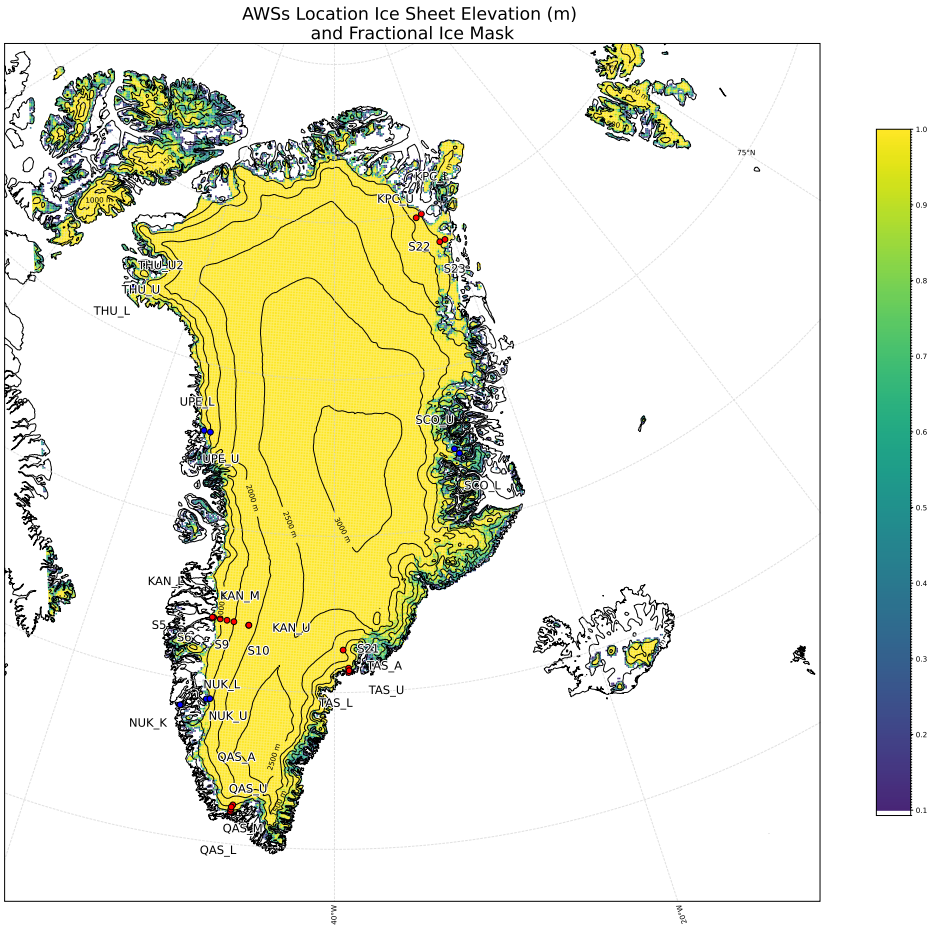

Figure 2.1: Map of the elevation of the GrIS (contour every 500m) and the location of PROMICE and IMAU AWSs. Stations in red are used to evaluate RACMO2.4p1 near-surface meteorology, SEB and SMB data, while blue dotted stations were used for the evaluation of RACMO2.4p1 SMB only.

Table 2.1: Description of AWS stations and modeled positions (Part 1). The second row for each station represents the modeled values.

Station	**Latitude (°N)**	**Longitude (°W)**	**Elevation (m a.s.l.)**	**Start Date**	**End Date**
S5	67.09	50.07	490	2003	2016
Modeled S5	67.09	50.01	585.44	–	–
KAN_L	67.10	49.95	670	01/09/2008	09/09/2020
Modeled KAN_L	67.09	50.01	585.44	–	–
S6	67.08	49.41	1020	2003	2016
Modeled S6	67.10	49.36	1049.97	–	–
KAN_M	67.07	48.84	1270	02/09/2008	12/09/2020
Modeled KAN_M	67.09	48.83	1287.11	–	–
S9	67.05	48.27	1520	2003	2016
Modeled S9	67.07	48.30	1472.61	–	–
S10	67.00	47.03	1840	2009	2016
Modeled S10	67.01	46.98	1856.07	–	–
KAN_U	67.00	47.03	1840	04/04/2009	08/09/2020
Modeled KAN_U	67.01	46.98	1856.07	–	–
KPC_L	79.02	24.08	370	17/07/2008	12/07/2019
Modeled KPC_L	79.89	24.13	397.68	–	–
KPC_U	79.83	25.17	870	17/07/2008	13/07/2019
Modeled KPC_U	–	–	–	–	–
QAS_L	61.03	46.85	280	24/08/2007	29/08/2020
Modeled QAS_L	61.04	46.87	437.75	–	–
QAS_M	61.10	46.83	630	11/08/2016	09/09/2020
Modeled QAS_M	61.10	46.79	645.49	–	–
QAS_U	61.18	46.82	900	07/08/2008	29/08/2020
Modeled QAS_U	61.20	46.82	979.51	–	–
QAS_A	61.24	46.73	1000	20/08/2012	24/08/2015
Modeled QAS_A	61.25	46.73	1073.03	–	–

Table 2.2: Description of AWS stations and modeled positions (Part 2). The second row for each station represents the modeled values.

Station	**Latitude (°N)**	**Longitude (°W)**	**Elevation (m a.s.l.)**	**Start Date**	**End Date**
TAS_L	65.64	38.90	250	23/08/2007	19/08/2020
Modeled TAS_L	65.64	38.95	263.78	–	–
TAS_U	65.70	38.87	570	15/08/2007	13/08/2015
Modeled TAS_U	65.69	38.83	586.23	–	–
TAS_A	65.78	38.90	890	28/08/2013	17/08/2020
Modeled TAS_A	65.79	38.95	980.03	–	–
S21	66.18	39.04	1615	2014	2017
Modeled S21	–	–	–	–	–
S22	78.91	22.38	535	2016	2020
Modeled S22	78.88	22.41	551.82	–	–
S23	78.92	21.44	142	2016	2020
Modeled S23	78.94	21.53	260.03	–	–

Directly measured variables from the AWSs are: air pressure (hPa), air temperature, converted to 2 meters height temperature (°C) for easy comparison to RACMO, relative humidity (%) conveerted to specific humidity at 2 m height, wind speed (m/s) also converted at 10m height wind speed, and wind direction (°); downward and upward short-wave and long-wave radiation, ice/snow surface height, subsurface temperature and GPS position (Fausto et al., 2021; Huai et al., 2020a) . From the measured variables, other variables are derived: specific humidity, sensible heat flux (SHF), latent heat flux (LHF), surface temperature, albedo; all equations are given in Fausto et al. (2021). In the calculation of SHF and LHF, uncertainties arise from the selection of the surface roughness parameter, which for the PROMICE AWSs is set to a constant value of z0=0.001 m which could overestimate the roughness over snow surfaces while underestimating it for rough ice, with possible consequent inaccuracies in the estimate of the turbulent heat fluxes (Fausto et al., 2021) . Given the difficulty of obtaining direct measurements for the turbulent heat fluxes and the different parameterizations used in the AWS models and in RACMO2.4p1, turbulent fluxes are usually the ones suffering the most when assessing models' performance (van Tiggelen et al., 2024a); however, it is still valuable to compare them to evaluate

how well the model represents temporal variations and patterns, such as seasonal or daily cycles, rather than focusing solely on the precise magnitudes.
Regarding the SMB, in-situ observations were used from the compilation of ablation measurements available at the PROMICE web portal (Machguth et al., 2016), which includes stake ablation and snow-pits point-measurements. Out of the 46 sites included in the database (Machguth et al., 2016), readings in locations where AWS data is used were employed, thus for the K-Transect (KAN and S5, S6, S9, S10 stations), Qassimiut Ice Lobe (QAS stations), the Kronpris Christian Land (KPC and S22-S23 stations), Isertoq Ice Lobe, close to Tasiilaq (where the TAS stations are located, close to where S21 is). Given the availability, also SMB at NUK, UPE and THU was evaluated to gain a more robust SMB evaluation from RACMO2.4p1, which is discussed later.

2.2.4 RACMO2.4p1 Data Treatment

RACMO2.4p1 data covers different aspects of the GrIS, hence the variables that were selected to be employed in this study are the SEB variables: SWd, SWu, LWd, LWu, SHF, LHF; near-surface meteorological variables: 2 m air temperature, 2 m specific humidity, 10 m wind speed; SMB and its components: melt, runoff, refreezing, retention, precipitation. The employed ice mask covers the continuous ice-sheet and the smaller ice caps at the margins that are not directly connected to it, so the computation of the integrated quantities also includes these ice caps.
Daily data was used to test RACMO2.4p1's ability of capturing daily meteorological variability. Scatter plots with the observed and modeled daily values of the near-surface meteorology and SEB variables are presented in the results. Time alignment was reached by matching the time-span of the modeled data to the time-span of the available observations for each AWS based on their specific activity period, as shown in tables 2.1 and 2.2 interpretations will follow in the Results section.
Monthly data was employed to study the differences between the modeled and the observed annual cycle of the SEB fluxes; shorter time-scales would have made the yearly cycle too noisy. The figures were realized by first removing from the model dataset of each variable the months that were not available from the observations, or the months that had less than 15 days of observations; then, for each variable, the monthly value of a given month was averaged with the monthly value of that month of all the available years, to obtain mean monthly-means of each month of the year representative of the whole dataset. Mean monthly-means of melt energy were also computed and plotted to relate it to the SEB cycle.
Time-series of the modeled and observed SMB were realized. The stations were

grouped per transect to show how the model can represent the differences from lower to higher stations. The entire available observed and modeled dataset is shown per AWS, referencing the length of the observational period. Yearly values from RACMO2.4p1 were computed by summing monthly SMB values and aligning the start and end of the year in RACMO2.4p1 to the hydrological year (from september to september (Hermann et al., 2018)), to better approximate the observed beginning and ending of the melting season. The last value of each annual RACMO2.4p1 SMB time-series was removed since it would be a sum of monthly data from september to december only of that year, since RACMO2.4p1 data starts each year on January and ends on December of that year. Also, in computing mean SMB yearly values from RACMO2.4p1, the modeled years were again aligned to the available observed ones. Since the SMB observational data was available for more locations where PROMICE AWSs are present (NUK, THU, UPE stations, the blue dots in Fig. 2.1), these were also employed. Therefore, time-series at the nearest grid-point for these stations were also extracted from RACMO2.4p1. However, AWSs data for SEB/near-surface meteorology was not available for those stations, and the model evaluation was not carried out for those variables. Modeled melt was also compared with observations for the same stations employed to study the SMB, and the same data treatment of computing and time-aligning modeled SMB to observed SMB was employed. Both SMB and melt were studied with respect to their change with elevation across the same transect, like at the K-Transect or the Q-Transect, and compared to the model's ability of portraying SMB and melt at the same region, presented in the results.

2.3 GrIS Integrated SMB and SMB components

The model was used to calculate the SMB integrated across the entire GrIS and surrounding ice caps evolution from 1945 to 2023, extending further back in time than the previous RACMO2.3p2 dataset. To do so, RACMO2.4p1 data in the spatial domain covering Greenland was used, and monthly SMB and SMB components values were first summed to get yearly values at each pixel, and then multiplied by the area of the pixels and summed across the whole mask to get yearly values, obtaining the integrated SMB and SMB components. To further the analysis, periods with the highest decreasing SMB rate were identified by calculating the slope and regression of SMB each 30 years (representing a climatological period) with a moving time window. This method found 1982 as the year of beginning of a series of climatological periods with SMB decreasing rates constantly higher than the SMB rates found in the climatological periods before 1982. Therefore, 1982 was chosen in this study as divide year between a period of SMB stability and a period of sharp SMB decrease.

This is slightly earlier than other studies found, for which this higher declining SMB rate starts in the 1990s (Fettweis et al., 2017; Hanna et al., 2011). Finally, maps were realized, by averaging the yearly SMB and SMB components over the last 30 years of RACMO2.4p1 (1993-2023) and over the first 30 years of RACMO2.4p1 data (1945-1975) to see how the SMB and SMB components changed spatially across the GrIS.

2.4 GrIS SMB variability and Summer GBI

2.4.1 Atmospheric Circulation over Greenland and the GBI

The atmospheric circulation above the GrIS is complex, the circulation patterns more relevant for the study of the GrIS SMB are those controlling the radiative fluxes and the inflow of warm and moist air masses. Greenland is located north of the North Atlantic Storm Track, where cyclons bring moist air to the southern and eastern part of the GrIS and enhance precipitation in the form of snowfall in those regions (Hanna, Hall, et al., 2018; Silva et al., 2022). Rossby waves breaks or other disruptions in the polar jet stream can cause a poleward steering of these cyclones or create high pressure systems (the so-called blockings) that transport anomalously warm and moist air towards the western part of the GrIS. Therefore, atmospheric dynamics impact in a spatially and seasonally differential way the SMB of the GrIS (Pettersen et al., 2022; Silva et al., 2022).

Different indexes can be used to represent the atmospheric circulation and pressure patterns above and in the vicinity of the GrIS. One of them is the NAO index, which is historically defined as the standardized difference in atmospheric pressure at sea-level between two points in the North Atlantic, the Azores and Iceland (Hanna et al., 2022), where 0.0 is the mean value and 1 is the standard deviation. Azores and Iceland are usually characterized by a persistent high-pressure for the first and a persistent low-pressure cell for the latter. However, their difference can be more or less strong, therefore defining a more or less strong latitudinal pressure gradient that affects the strength of the polar jet stream, making the NAO more positive when the jet stream stronger and more negative when the jet stream is weaker. The NAO can also be defined through Principal Component Analysis (PCA) to remove bias from local anomalies and implement its calculation with spatial values that improve its representation, since the center of action of the NAO can vary spatially with varying climatic conditions (Hanna et al., 2022). Given its relation to pressure systems and the polar jet stream, the NAO is found

to negatively correlate with high summer melt and the observed SMB decrease of the last decades, for which a more persistent negative phase of the NAO has been observed (Fettweis et al., 2013; Hanna et al., 2022).

Another important index to which the NAO is negatively correlated to is the Greenland Blocking Index (GBI). The GBI has been chosen for this study for its more precise spatial range of definition (Hanna et al., 2013). The GBI is defined as the mean geopotential height at 500 hPa in the area between 60–80°N and 20–80°W (Hanna et al., 2013), thus it more closely captures air circulation changes specific to Greenland, while still being correlated to the NAO. The GBI is a measure of the atmospheric blockings occurring in the vicinity of Greenland. To give a more precise description, blockings are large-scale (hundreds of km wide) quasi-stationary (few days to weeks or longer) anticyclonic systems (flowing clockwise in the northern hemisphere) forming in the mid-troposphere that deflect the normal zonal flow of westerly winds and cyclones in the North Atlantic Storm Track, both upstream and downstream of the block Pettersen et al., 2022. High GBI values are associated with a suppression of cloud cover and an increase of warm air advection to the western part of Greenland, thus increasing incoming short-wave radiation and sensible heat flux towards the surface, leading to higher surface melt (Ward et al., 2020). Figure 2.2 shows the general circulation above the GrIS and how it changes in a high or low summer GBI, with 500 hPa geopotential height, wind speed and direction, temperature and total cloud cover. The means were computed over 30 years of ERA5 data (1991-2021), while the anomalies were computed by subtracting the mean of the variables for the high (low) summer GBI years from the climatological mean, where high (low) summer GBI years are defined as years for which the mean summer GBI is at least 1σ higher (lower) than the mean summer GBI (the dataset employed for the GBI values is described in the following section). High summer GBI leads to positive temperature anomalies over the GrIS and especially in its central part, while cloud cover decreases with higher negative anomalies in the eastern part of the GrIS; cloud cover increases in the southern tip of the GrIS. On the contrary, when summer GBI is low, air temperatures decrease over the ice sheet and cloud cover shows a positive anomaly, stronger in the eastern part of the GrIS. The GBI strongly correlates with summer melt and the overall trend of decreasing SMB through the said alteration of SEB variables (Fettweis et al., 2013; Hanna, Hall, et al., 2018; Hofer et al., 2017; Huai et al., 2020b), and the correlation between SMB, summer melt and summer GBI will be further discussed in the following sections.

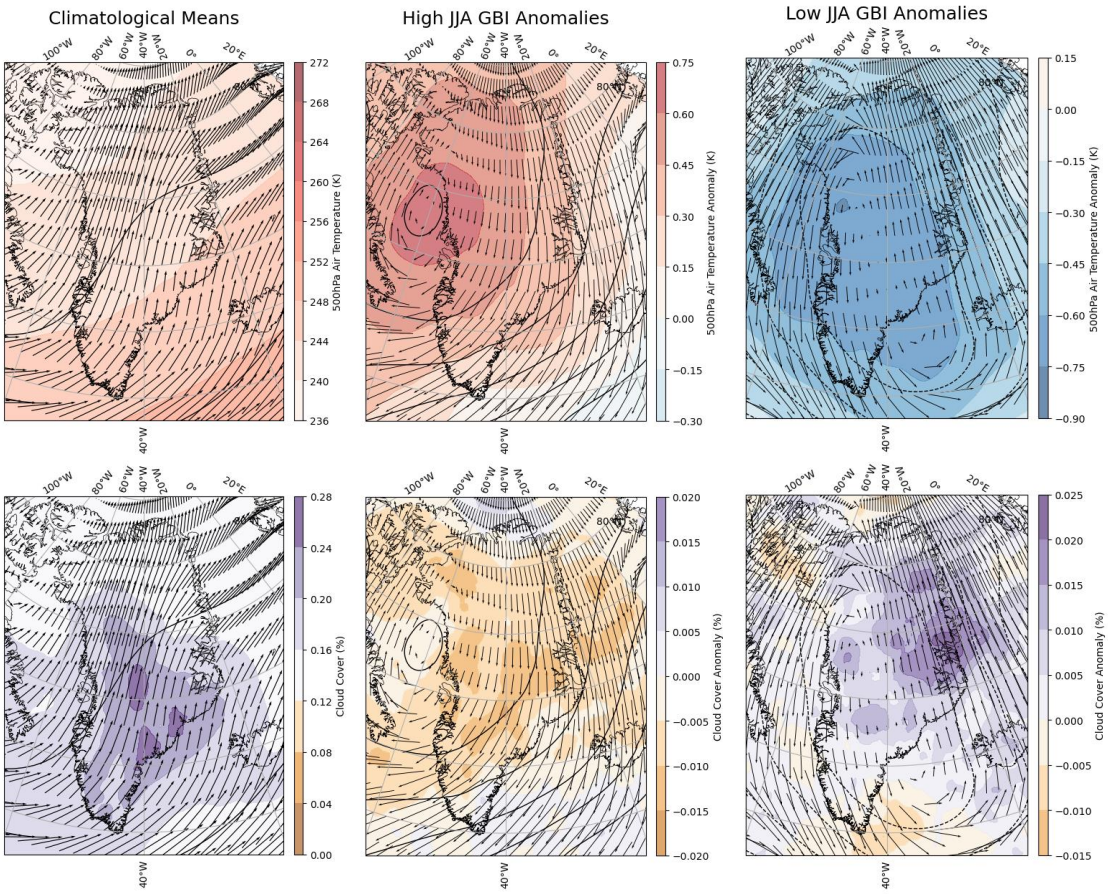

Figure 2.2: Mean atmospheric circulation over Greenland and circulation anomalies for high and low JJA GBI years computed over 30 years of ERA5 data (1991-2021). Climatological means are in the first column, while high JJA GBI and low JJA GBI years in the second and third. First and second row show wind direction and 500 hPa geopotential height with surface temperature in the first row and total cloud cover in the second.

2.4.2 GBI dataset description

The dataset used in this study was produced by Hanna et. al (2016) last updated in 2023 (until september) and maintained at the NOAA Physical Science Laboratory (PSL). The dataset includes monthly GBI values from the NCEP/NCAR Reanalysis and the Twentieth-Century Reanalysis version 2c (20CRv2c) data from 1851 to 2023,

and is based on means of the GBI monthly anomalies standardized to the 1951-2000 period (Hanna et al., 2016). The data is then unitless since the GBI anomalies for each month were divided by its standard deviation, and values range between ca. +- 2.

2.4.3 SMB, SEB and GBI

To correlate SMB/SEB variables to the GBI, first GrIS integrated SMB values were used. Summer GBI values were computed (JJA) and correlated to the annual SMB and melt calculating Pearson correlation coefficients and R^2 values to quantify the strength of the linear relationships; values of the slope are also shown in the figures presented in the results, representing the change in annual SMB caused by a change in JJA GBI.
Secondly, spatial differences in the response to summer GBI across the ice sheet were studied. Spatial correlation and slope maps were realized on a pixel by pixel basis, for which annual SMB and SMB components and the summer-averaged SEB variables at each pixel were regressed against the JJA GBI time-series, to realize maps of the correlation and slope between the GrIS SMB/SEB and the JJA GBI. The slope represents the change in the SMB/SEB variable for a one-standard-deviation change in summer GBI (σGBI). Therefore, the calculated slope provides a measure of the rate of change in the SMB/SEB variable with respect to GBI variability. Annual values were considered for SMB, melt, runoff, refreezing and retention since their annual values depend on their summer values and only occur when melting occurs, which is mainly in summer. In addition, SMB refers by definition to the annual balance between input/output mass fluxes. Therefore, all mass fluxes were considered in their annual sums. Melt was also converted in terms of energy flux via the latent heat of fusion:

$$E_{melt} = melt * \rho_{ice} * L_f \tag{2.6}$$

Where melt is in mm w.e. (equivalent to kg m^{-2}), ρ_{ice} is 917 kg/m^3 and the latent heat of fusion (L_f) is 3.34e5 J/kg, obtaining melt energy (E_{melt}) in Wm^{-2} . This way, the correlation and slope maps of the SEB variables presented in Wm^{-2} can be directly compared to the values obtained for the JJA SEB variables.

Chapter 3

Results

This chapter presents the results divided into the three main research questions: (1) model evaluation; (2) GrIS integrated SMB reconstruction with RACMO2.4p1; (3) correlation between SMB/SEB and GBI.

3.1 Model evaluation

3.1.1 SEB Variables

Figure 3.1 compares observed and modeled SEB variables for all AWSs. The radiative fluxes (SWu, SWd, LWu, LWd) are in good agreement with observations, all having a bias < 10 W/m^2 (apart from LWd) . The bias in SWd is 0.2 W/m^2 with a RMSE of 39.2 W/m^2, while for the SWu the bias is 3.2 W/m^2 and the RMSE 34.4 W/m^2. Both SWu and SWd bias values are within the measurement error (10%), so RACMO2.4p1 is accurate within measurement accuracy (van Dalum et al., 2021; van Tiggelen et al., 2024b). The presence of many non zero modeled values while the observed SWd or SWu is equal to zero, can be explained by the snow covering the sensors in some locations that hinders the ability of the sensors of measuring shortwave radiation. The correlation coefficients (R^2) for SWd and SWu are 0.91 and 0.85, respectively. The LWd bias is -16 W/m^2 with a RMSE of 25.4 W/m^2 and an R^2 of 0.72, while the LWu is slightly more accurate, with a bias of -6.6 W/m^2, RMSE of 11.76 W/m^2 and R^2 equal to 0.92.

The turbulent heat fluxes are not well represented in RACMO2.4p1 and their bias and RMSE are higher: the SHF has a bias of 1.9 W/m^2 with RMSE of 21.7 W/m^2 and an R^2 of 0.45, while the LHF has a bias of 4.6 W/m^2 and a RMSE of 11.3

W/m^2, and a slightly larger R^2 of 0.52; these results can be compared to how well RACMO2.4p1 captures the near-surface meteorology. Figure 3.2 shows plots for air temperature, wind velocity and specific humidity at 2 m, while surface temperature is not since is constant. The three plots show a very good agreement between observations and the model, thus not serving a straightforward explanation as to why the turbulent fluxes are so poorly simulated, which will be further addressed in the discussion.

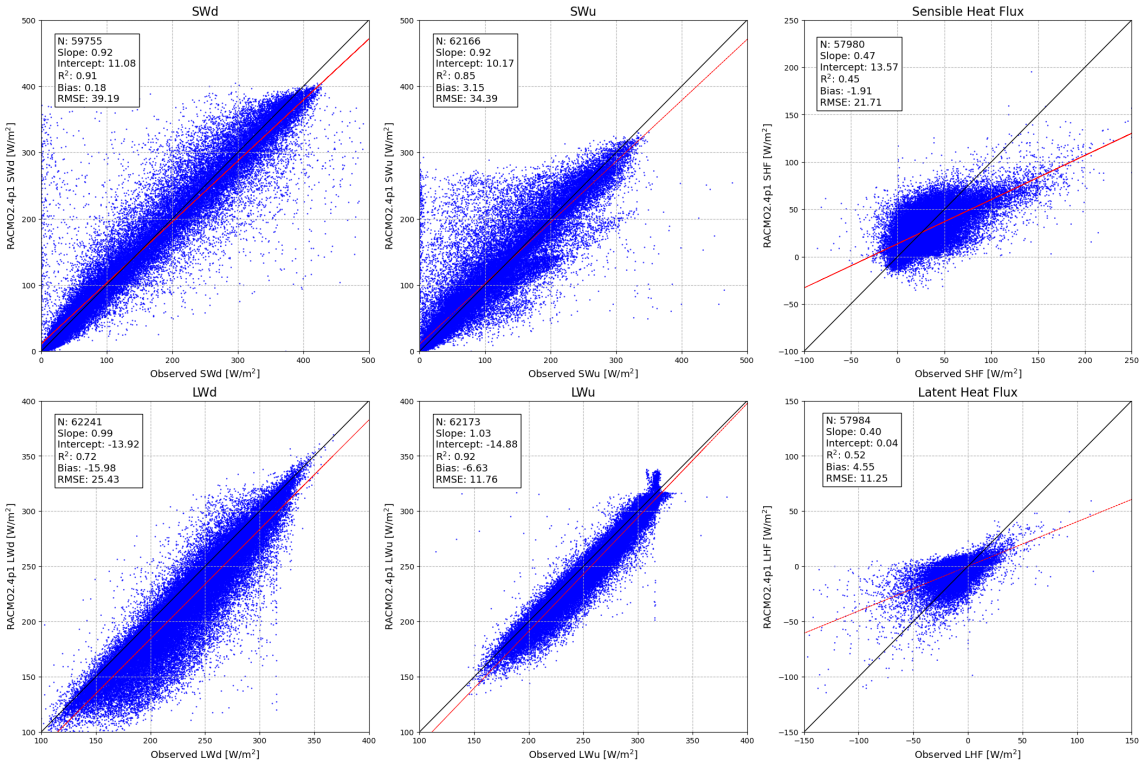

Figure 3.1: Scatter plots for daily averaged observed vs. RACMO2.4p1 modeled SEB variables: shortwave down, shortwave up, longwave down, longwave up and the sensible and latent heat flux. The number of observations (N), determination coefficient (R^2), root-mean-squared-error (RMSE) and bias are shown in the figures.

As a complement to the scatter plots shown above, monthly averages from the AWSs daily observations and from RACMO2.4p1 were used to see how well the seasonal SEB cycle is portrayed by RACMO2.4p1. In Figure 3.3, the yearly cycle of the mean-monthly means of SWnet, LWnet, SHF, LHF, Gs and melt energy (computed

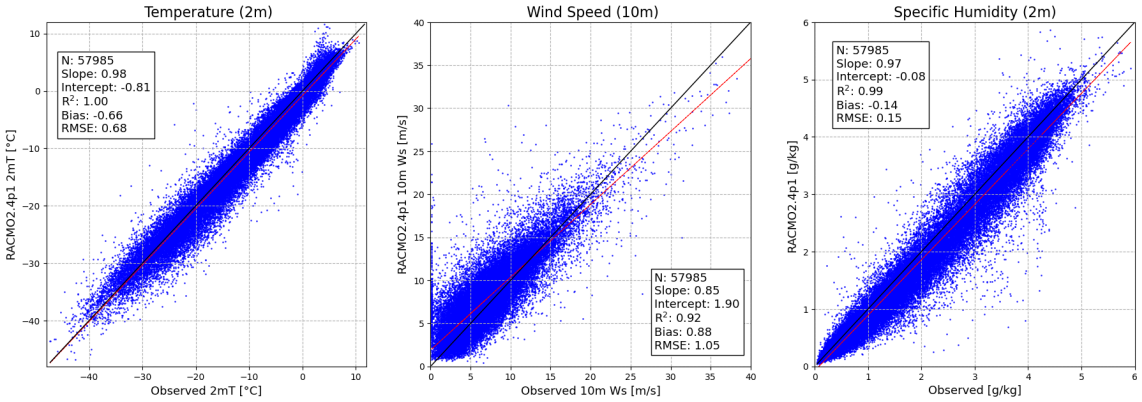

Figure 3.2: Scatter plots for daily averaged observed vs. modeled from RACMO2.4p1 near-surface meteorological variables: 2m height air temperature, wind speed at 10m and 2m height specific humidity (g/kg); the number of observations (N), determination coefficient (R^2), root-mean-squared-error (RMSE) and bias are shown in the figures.

from the melt flux available in the RACMO2.4p1 output using the latent heat of fusion) is shown for the stations along the K-transect. Melt energy is mostly well simulated by RACMO2.4p1, however, at most stations it is slightly underestimated due to over-/underestimation of the different energy fluxes. Station S5 and similarly, KAN_L, show that the net short-wave radiation is overestimated during summer by RACMO2.4p1, while the SHF is underestimated. Therefore, the two biases have a compensating effect and the melt energy is slightly underestimated at both stations. At station S6, the SHF is in agreement with the observed values throughout the year. However, the netSW is overestimated by 20-30 W/m^2 in July so that the melt energy is overestimated by around 10-20 W/m^2, which can be explained by the small underestimation of the netLW radiation. For station S9, both netSW and netLW are slightly underestimated, and melt is also underestimated. Station KAN_U presents very good agreement throughout the seasons for all energy fluxes. S10 and KAN_U are at the same location hence the over/under-estimation of fluxes is also controlled by observational biases. In general, throughout the K-Transect, the difference between the observed and the modeled seasonal energy fluxes decreases going from the lower to the higher stations, a pattern visible for the Q-Transect and the other regions as well; see the discussion. Another visible pattern, is the delayed modeled increase in SWnet that occurs at the beginning of the melting season in Apr/May at stations KAN_U, S5 and other stations such as QAS-M and TAS-L which are

low-elevation stations. At these locations, the net shortwave radiation modeled in RACMO2.4p1 is lower than the observed from February until May/June, then, during the melting season, the modeled net short-wave fluxes are overestimated by the model. The possible reasons for this are further explored in the discussion, but seem to be mainly due to an overestimation/underestimation of surface albedo. Regarding the turbulent heat fluxes, the high spread of SHF in the bias plots is visible in the yearly cycles as well: low-stations have a summer SHF that is underestimated by RACMO2.4p1 while higher-elevation stations (like S9, KAN_U, S10, KAN_U) have a well modeled summer SHF, but the SHF during winter is overestimated. Other fluxes are better represented: the difference between modeled and observed netLW is lower even though RACMO2.4p1 seems to underestimate it throughout the year for all AWSs, in agreement with the scatter plots. LHF and the subsurface conductive heat flux are also close to observations.

3.1.2 Surface Mass Balance and Melt

The SMB appears to be overestimated by RACMO2.4p1 with respect to observations at all stations, as shown in figure 3.4, where data points tend to cluster above the 1:1 line. The bias is 1, the RMSE is 0.7 and the R^2 is 0.65 m w.e./yr, which leaves 35% of the variability unexplained by the model with an average overestimation of the mean observed SMB. However, for some AWS, RACMO2.4p1 represents the mean SMB almost perfectly, like at station S6, UPE_L, KAN_M, S9, KPC_U, KPC_L.

Regarding station-specific SMB values, Figure 3.5a shows that the greater discrepancies between observations and RACMO2.4p1 values are present at the lower stations, KAN_L and S5 (considering however that both stations are modeled in the same pixel for RACMO2.4p1). The difference between modeled and observed yearly SMB per station is shown also in the bias (as difference between the mean modeled values and mean observed mean values per station over all years) in Figure 3.5b where S5 has the greatest bias, -0.92 m w.e., so RACMO2.4p1 underestimates the SMB at this station, i.e. simulates it to be less negative. The bias decreases with elevation, with the lowest value of 0.08 m w.e. at S9. The ability of RACMO2.4p1 of representing the SMB is also related to how well it can represent melt, which shows the same pattern of a bigger discrepancies for the lower stations, and is overall underestimated, which could explain the overestimated SMB. The mean observed and modeled yearly melt values are shown in the Table 3.1, where the stations are divided into their region and placed in order of elevation, to show how much the modeled melt becomes closer to the observed one when going from the lower to the upper stations.

Figure 3.3: The mean-monthly means for net shortwave, net longwave, SHF, LHF, Gs and melt energy are portrayed in the figure, comparing observations to RACMO2.4p1. The means were computed by removing from the observational dataset months with less than 15 days of observations and the corresponding months from the model dataset for time-alignment (see Methods). The dashed lines are the modeled values while the solid colored lines represent the observational data.

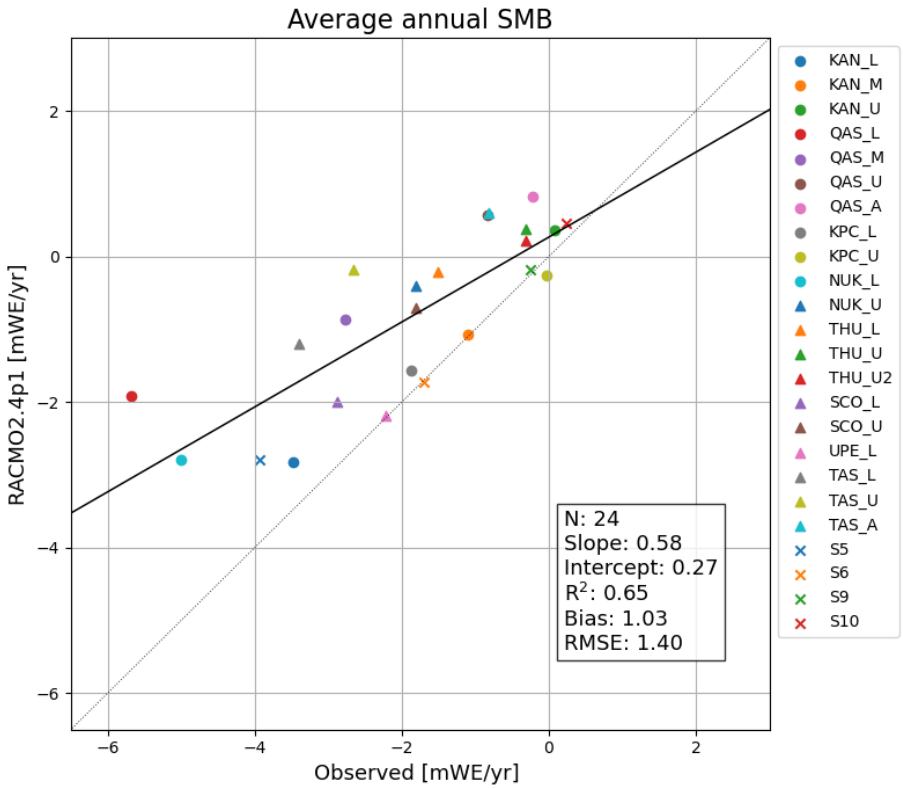

Figure 3.4: Observed on the x-axis vs. RACMO2.4p1 yearly SMB values on the y-axis for all AWS (also the ones added for which SMB data were available, UPE, THU, NUK and SCO) with the one-to-one line and the black line which represents the regression line between the two datasets. The slope, intercepet, R^2, Bias and RMSE values are also shown in the figure.

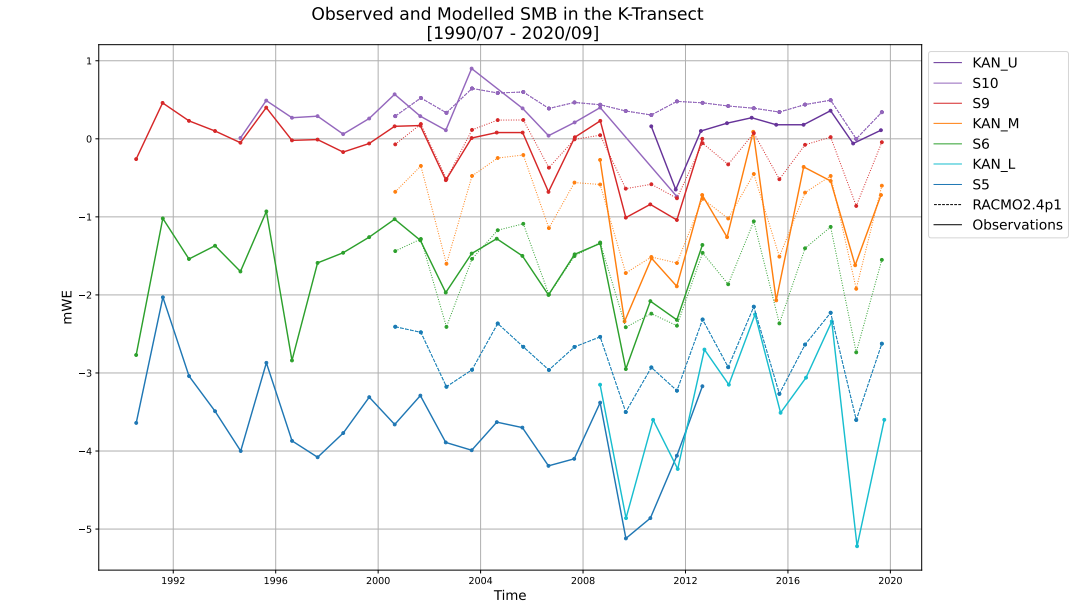

(a)

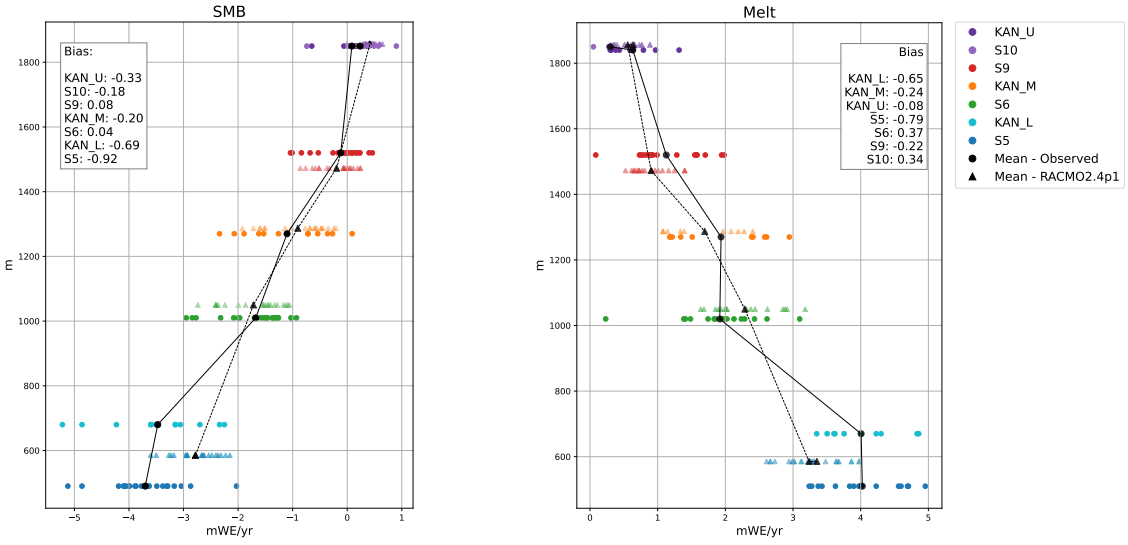

(b) (c)

Figure 3.5: Annual SMB along the K-Transect. SMB change during the years of available data (panel a); yearly SMB values as a spread around the mean for the different AWS against their elevation (panel b). Yearly melt for that AWS against the modeled and observed elevation (panel c).

Table 3.1: Difference between modeled and observed mean annual melt at AWSs with mean bias

AWS	Observed Melt (m w.e.)	Modeled Melt (m w.e.)	Bias
S23	2.56	1.26	-50.78
KPC_L	2.19	1.12	-48.86
S22	1.42	1.10	-22.54
KPC_U	0.61	0.67	9.84
QAS_L	6.03	3.44	-42.96
QAS_M	3.48	2.49	-28.45
QAS_U	2.36	1.68	-28.81
QAS_A	2.24	1.56	-30.36
TAS_L	3.61	1.69	-53.19
TAS_U	3.26	1.59	-51.23
TAS_A	2.40	1.33	-44.58
S21	0.54	0.77	42.59
S5	3.97	3.22	-18.89
KAN_L	3.81	3.23	-15.23
S6	2.03	2.27	11.82
KAN_M	1.86	1.67	-10.22
S9	1.66	1.17	-29.52
S10	0.36	0.61	69.44
KAN_U	0.57	0.52	-8.77

So far, RACMO2.4p1's ability of representing SEB variables, near-surface meteorology and SMB and melt for the selected AWSs seems to be successfully capturing temporal patterns and spatial variability, but with the tendency of underestimat-

ing melt and overestimating the SMB, especially in the lowest ablation regions. For SMB, the small bias (1 m w.e.) and the high R^2 =0.65 m w.e. allow for the use of the model for integrated SMB reconstructions, while acknowledging its limitations and deviations that may arise from local processes. The following part will present results of the SMB integrated across the whole GrIS from 1945 to 2022 and its correlation with the Greenland Blocking Index (GBI).

3.2 Greenland Ice Sheet Integrated SMB

The SMB of the entire GrIS was studied by integrating the SMB and components (runoff, accumulation, melt and refreezing) through the GrIS area, as explained in the methods. Figure 3.6 presents the results, highlighting the variability of the SMB and its components from 1945 to 2023. As mentioned, the reconstruction goes further back in time with the use of the ERA5 compared to previous RACMO simulations. The SMB decreases from 1945 to 2023 with a rate of -0.7 +- 0.6 Gt/yr^2, which accelerates from the 1980s reaching values of -3.8 +- 1.4 Gt/yr^2 from 1982 to 2023. Accumulation has increased too little to offset the strong increase in surface melt and runoff. In fact, accumulation changed at a rate of 0.4 +- 0.4 Gt/yr^2 from 1945-2023 while from 1982 to 2023 its slope decreased (0.14 +- 1 Gt/yr^2)). However, runoff has been increasing by 1.7 +- 0.4 Gt/yr^2 from 1945-2023 and more than doubled from 1982-2023 up to 4.2 +- 0.9 Gt/yr.

Spatial differences are shown in Fig. 3.7, where first the average SMB throughout the whole time-span is shown and secondly the differences between the recent and early selected periods for the SMB and its components. In the SMB map, the values where accumulation and ablation are balanced correspond to the Equilibrium Line Altitude (ELA) which is marked by white values. On average, the SMB is most positive in SE Greenland, while it is negative along the ablation zone in the western GrIS and in the North and North-Eastern parts. The SMB became increasingly negative towards the most recent period, especially along the margins, where runoff increased most (Fig. 3.8a). While melt increased also in higher-elevation areas of the ice sheet, runoff increased specifically in the ablation regions: this is because refreezing increased strongly at the higher elevations, where also melt increased, and it decreased in the regions where runoff increased, along the ablation parts of the ice sheet, while maintaining on average the same values along the ELA. Precipitation increased in NE Greenland and along the western part, while it decreased in the southern tip and along the Q-Transect (Fig. 3.8b).

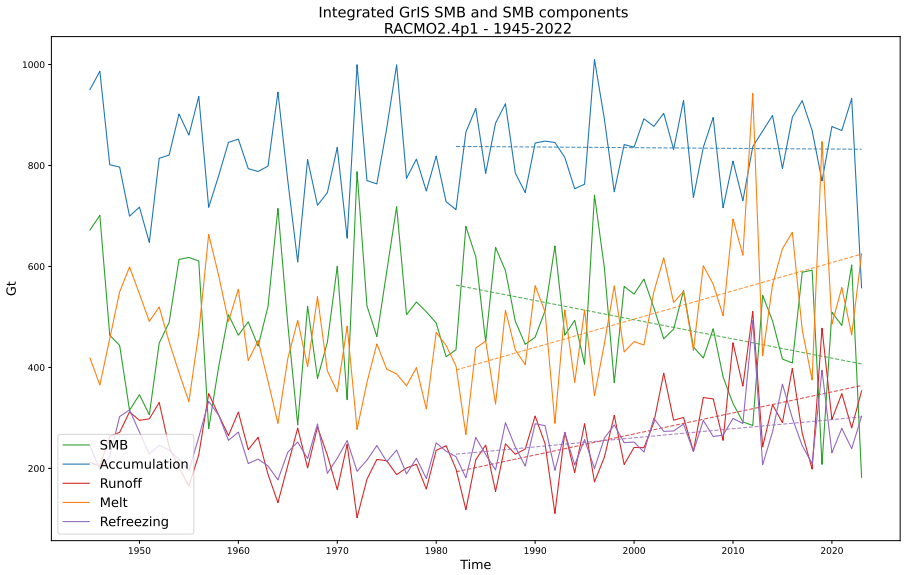

Figure 3.6: GrIS and disconnected ice caps integrated SMB and SMB components from 1945 to 2023 using RACMO2.4p1 data and regression lines from 1982 to 2023.

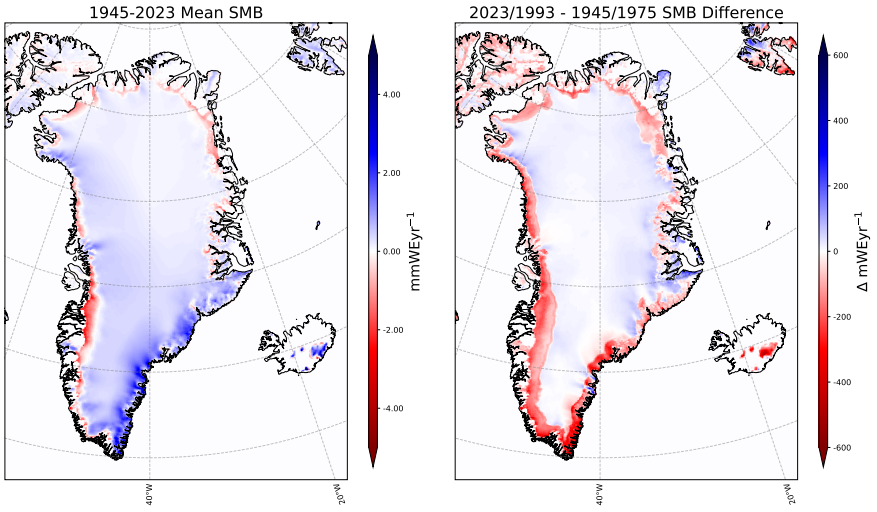

Figure 3.7: Mean GrIS RACMO2.4p1 SMB and the difference between 1993-2023 and 1945-1975 means.

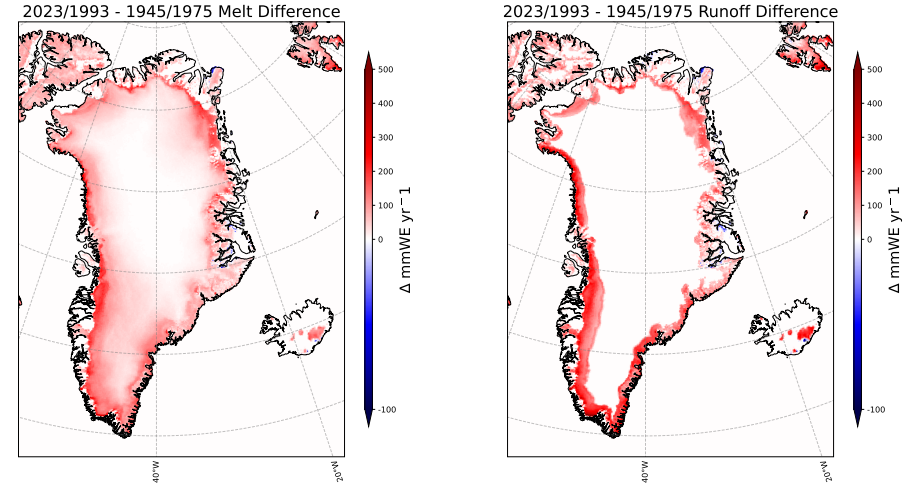

(a)

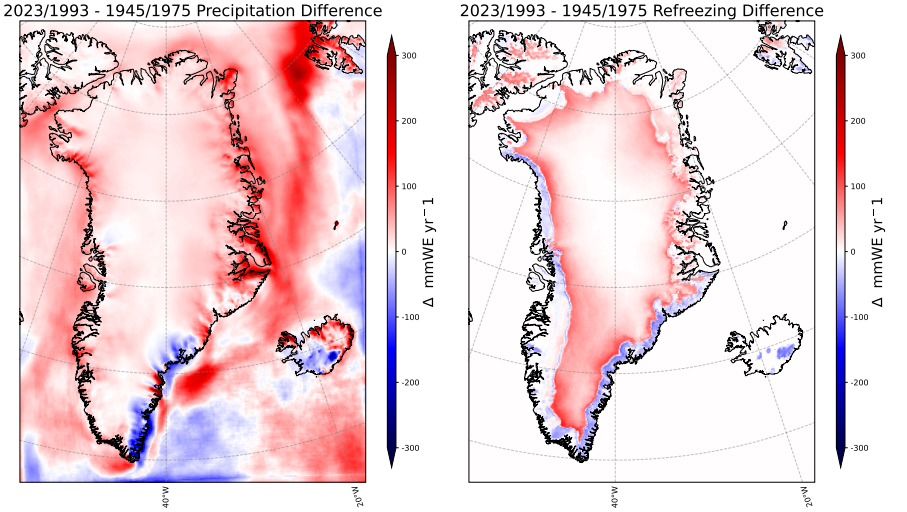

(b)

Figure 3.8: (a) Difference in the recent and early average melt and runoff; (b) difference in early and recent precipitation and refreezing.

3.3 Greenland Blocking Index and Surface Mass Balance

3.3.1 SMB, GBI and Melt Connections

The relationship between the GrIS SMB and the GBI was examined with qualitative and quantitative methods. Fig. 3.9 presents in the first panel the time series of annual SMB alongside summer and winter GBI, highlighting their inter & intra-annual variability. The second panel displays scatter plots of annual SMB against JJA and DJF GBI, with regression lines and corresponding statistics. The analysis showed a stronger anti-correlation between annual SMB and JJA GBI, with a R=-0.67 and an R^2=0.44, while R=-0.20 and R^2=0.04 with the DJF GBI. The third panel shows the relationship between annual SMB and summer melt, for which R=-0.75 and R^2=0.57. This indicates that while the annual SMB is influenced by multiple components, summer melt serves as the main driver. This is confirmed in the fourth panel, which shows the connection between summer melt and summer GBI, showing a strong positive correlation (R=0.85, R^2=0.72). This result bridges the relationship between annual SMB and summer GBI, demonstrating that summer GBI exerts its influence on SMB primarily through its impact on summer melt.

3.3.2 Spatial correlations

The correlation map of SMB (Fig. 3.10a) shows that the annual SMB is especially anti-correlated in the marginal parts of the ice-sheet, with higher correlation values found in the entire western part of Greenland. High negative values are found in the north and north-eastern part as well, while the anti-correlation decreases along the south-eastern tip of the ice-sheet. The only part of the ice sheet that seems weakly positively correlated to summer GBI is in the interior, in the NE part of Greenland, where the annual SMB slightly increases when summer GBI increases. Similar regional differences of correlation can be found for the precipitation, which is weakly negatively correlated to summer GBI, apart from NE Greenland, where the correlation is slightly positive. The spatial correlation of melt is positive everywhere on the GrIS, and it is less strong going within the interior parts of the ice-sheet. Runoff has a strong positive correlation from the ELA down to the ice-sheet margins; on the contrary, refreeze and retention have a negative correlation where runoff is positive. In the rest of the ice-sheet retention and refreeze have a positive correlation with summer GBI. The sensitivity of the annual SMB and SMB components to summer GBI, as shown in Fig. 3.10b, follows the spatial patterns of their correlation. The

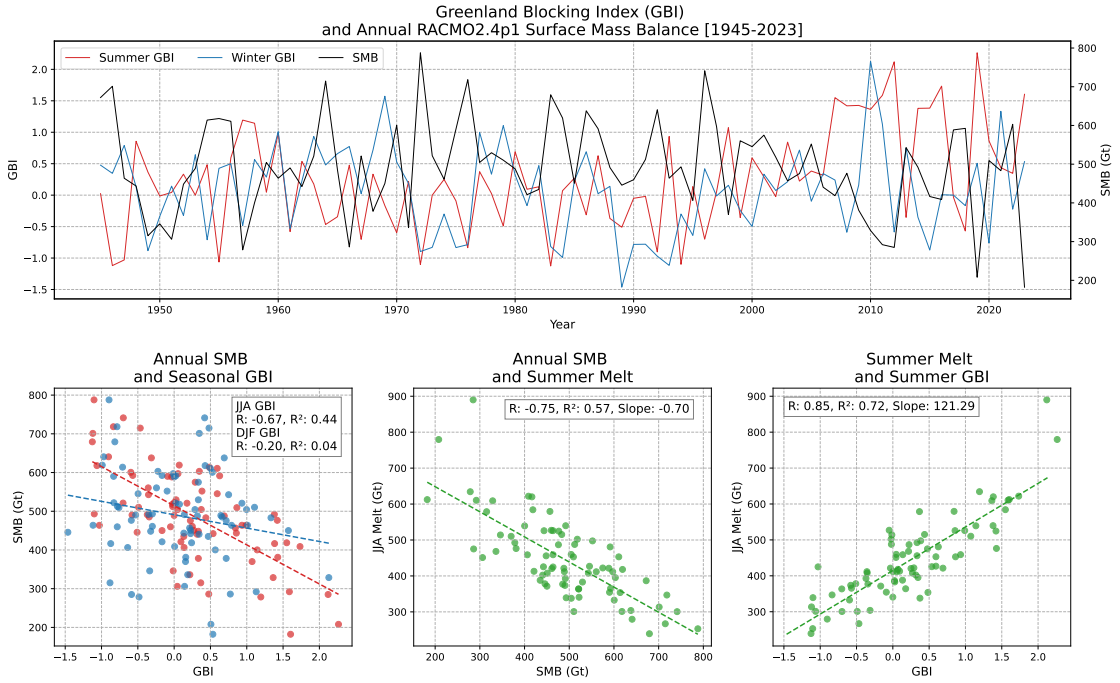

Figure 3.9: Annual SMB and DJF-JJA GBI from 1945 to 2023 are shown in the upper panel; the bottom subplots represent the correlation between 1. annual SMB and winter and summer GBI; 2. annual SMB and summer melt; 3. summer melt and summer GBI. Pearson correlation values and values for the R^2 are given as well.

annual SMB decreases up to 400 mm w.e. per year when the summer GBI increases of 1σGBI in the south and western part of the ice-sheet, which are the regions where melt and runoff show the higher sensitivity, up to 400 mm w.e. Precipitation, refreeze and retention have a smaller sensitivity but follow a similar spatial pattern for which when the summer GBI increases, they both increase at higher elevations and decrease below the ELA, even though values are close to zero and their decrease is not high.

To explain these correlations, the spatial variability of summer SEB components (SWu, SWd, netSW, LWd, LWu, netLW, LHF, SHF) to summer GBI was studied, and the results point to an increase of netSW radiation caused by a decrease in the SWu radiation (Fig. 3.11b). Other fluxes are not strongly affected, as shown in the Figure. The relation between these spatial patterns will be explored in the discussion.

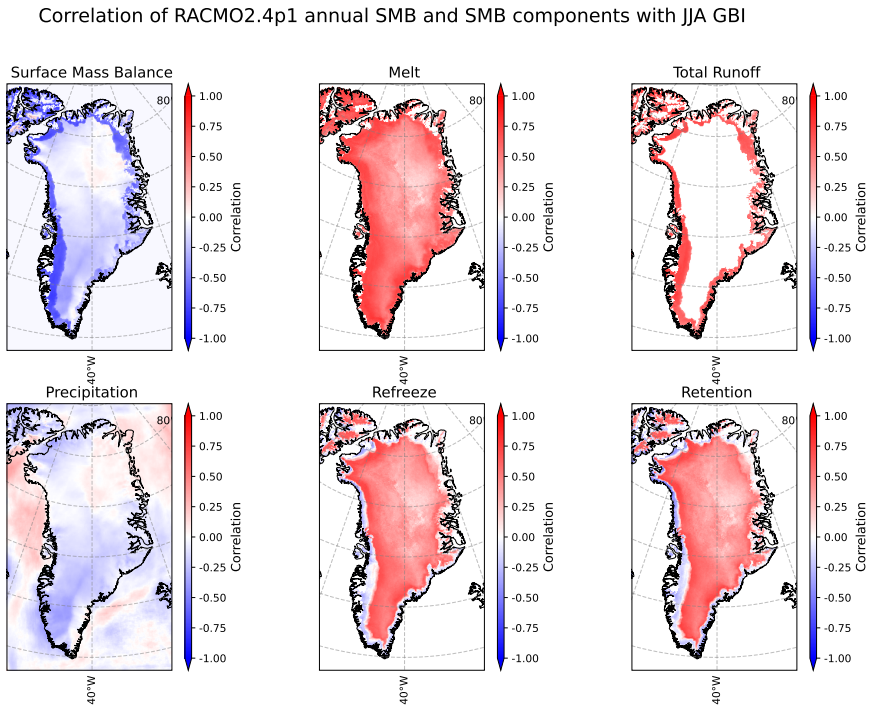

(a)

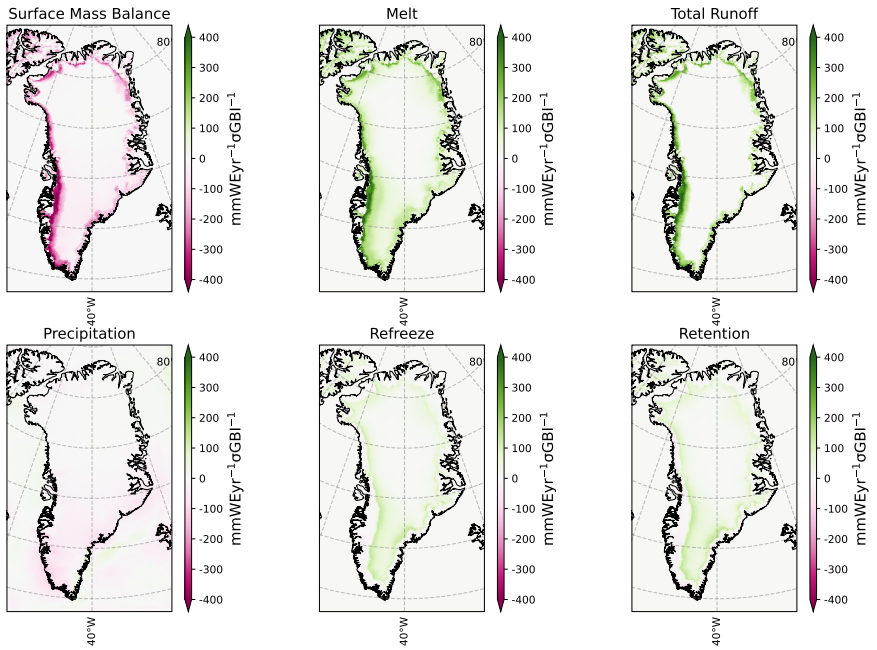

(b)

Figure 3.10: Correlation (a) and sensitivity (b) of the annual SMB and other annual SMB components (runoff, melt, precipitation, refreeze and retention) to the summer GBI; changes in the variables are in mm w.e./yr and correspond to an increase of 1σGBI over summer (JJA).

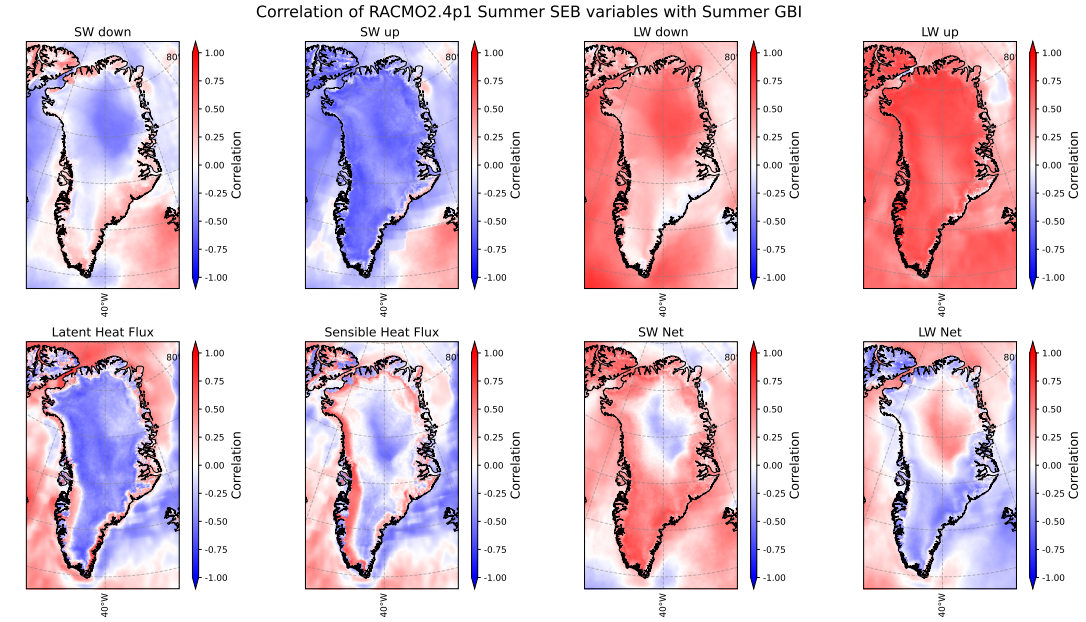

(a)

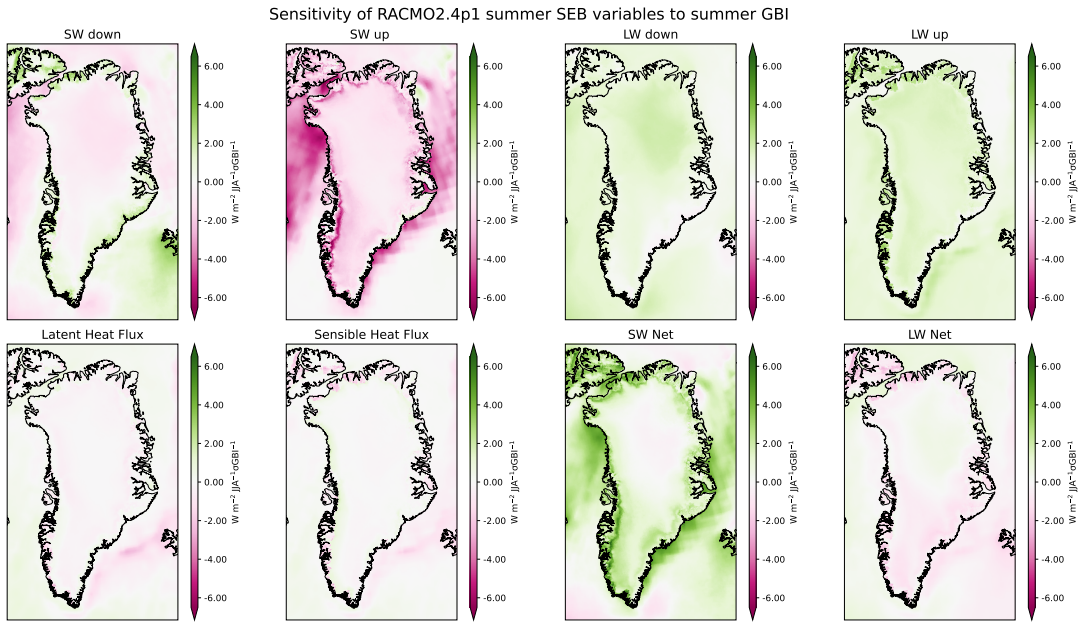

(b)

Figure 3.11: Correlation (a) and sensitivity (b) of the summer mean SEB variables (SWd, SWu, netSW, LWu, LWd, LHF, SHF) to the summer GBI; changes in the variables are in W/m^2 and correspond to an increase of 1σGBI over summer (JJA).

Chapter 4

Discussion

This chapter tries to identify processes and caveats: why the model over-/underestimates energy fluxes, how it is related to the SMB computation at the different AWSs, and why RACMO2.4p1 is a reliable source for the GrIS integrated SMB. The variability of the integrated SMB and SMB components with respect to the GBI will be discussed and the atmospheric conditions inducing higher summer melt when JJA GBI values increase will be also explained.

4.1 Model Evaluation

SEB variables (SWnet, LWnet, SHF, LHF) determine the available melt energy at the surface of the GrIS, which controls the runoff flux and the SMB. RACMO2.4p1 represents the near-surface meteorology well, with small biases. SEB variables present more issues, with the overestimation of the SWd, SWu, LHF, and the underestimation of the LWd, LWu and SHF. The values are summed up in Table 4.1, where R^2, bias and RMSE of RACMO2.4p1 vs. observations at the 19 AWSs for daily values are shown, along with the R^2, bias and RMSE from Noël et al. (2018) for RACMO2.3p2; note that 4 additional AWSs were considered which are not considered here and SHF and LHF were not studied. R^2, bias and RMSE values from van Dalum et al. (2024) for RACMO2.4p1 are also presented, with the 11 km ice-mask and the additional UPE_U and NUK_U AWSs, while S22 and S23 were not considered. Therefore, the values in the table are presented as a qualitative measure of RACMO2.4p1-5.5km's improvements from previous versions, with the acknowledgment that a thorough comparison with the same data filtering criteria and selection of the same AWSs is necessary to further constrain its refinements. Some are, however, already visible, i.e. the 2 m air temperature and the 2 m

specific humidity from RACMO2.3p2. However, the turbulent heat fluxes have not improved, which can be due to the high sensitivity to data errors in calculating SHF and LHF and to the lower filtering applied in this study to observational data. Possible problems with albedo, cloud cover and other parameters are discussed below to try and explain RACMO2.4p1's SEB and SMB variables representation.

AWS Variable	RACMO2.4p1-5.5km			RACMO2.4p1-11km			RACMO2.3p2-11km		
	R^2	Bias (W/m^2)	RMSE (W/m^2)	R^2	Bias (W/m^2)	RMSE (W/m^2)	R^2	Bias (W/m^2)	RMSE (W/m^2)
2mT	1.00	-0.66	0.68	0.99	-0.63	2.18	0.95	-0.1	2.4
2mQ	0.99	-0.14	0.15	–	–	–	0.95	0.1	0.4
10mWs	0.92	0.88	1.05	0.94	-0.39	1.77	0.68	-0.02	2.0
SWd	0.91	0.18	39.19	0.99	-0.60	24.5	0.95	3.8	27.1
SWu	0.85	3.15	34.39	0.98	-4.47	28.1	0.88	6.8	32.1
LWd	0.72	-15.98	25.43	0.96	-14.5	24.3	0.83	-7.1	21.2
LWu	0.92	-6.63	11.76	0.99	6.56	11.4	0.92	-4.4	12.1
SHF	0.45	1.91	21.71	0.86	0.28	19.0	–	–	–
LHF	0.52	4.55	11.25	0.85	4.84	10.5	–	–	–

Table 4.1: R^2, bias and RMSE between different RACMO versions and AWSs data. The first column shows RACMO2.4p1 with the 5.5 km resolution ice-mask and the selected 19 AWSs for this study; the second one presents values from van Dalum et al. (2024), where RACMO2.4p1 data was obtained using the 11 km ice-mask; last column has values from Noël et al. (2018), which used RACMO2.3p2.

Albedo and Snowfall

The background bare ice in RACMO2.4p1 is set as constant value from MODIS (van Dalum et al., 2024), while the snow albedo is implemented by translating it into its impurity content. The bias plots and annual SEB fluxes cycle suggest that the SWnet is underestimated, especially at lower lying stations, which have higher ablation rates. This netSW underestimation is mostly dependent on the overestimation of SWu, which is in turn caused by an overestimation of the surface albedo. However, albedo values for the bare ice seem to be correct and in accordance with observation: when the snow cover is completely removed, the netSW modeled by RACMO2.4p1 matches the observed one at station S23 for example, or at station S6, S10, KAN_L, meaning that the bare-ice albedo has realistic values. Therefore, overestimation of the surface albedo is more probably an overestimation of snowfall during winter. In fact, snowfall overestimation, delays the onset of the ice ablation season and explains the higher albedo values observations, because bare ice is exposed later on in the model. This is especially visibile at QAS_L, where the modeled yearly netSW cycle does follow the observations; however, the modeled netSW peak is delayed in RACMO2.4p1,

therefore the SWu is higher than it should for a longer period, meaning that it takes longer for the model to remove all the snow covering the ice accumulated during winter/spring. The Qassimiut ice lobe, where the QAS stations are located is notably difficult to model (Hermann et al., 2018), due to the high observed snowfall rates. A similar pattern is visible for S5, however, the albedo overestimation could be in this case also caused by the inability of MODIS to represent the heterogeneity of this area (Huai et al., 2020a; Noël et al., 2018). An overestimation of snowfall is plausible since RACMO2.4p1 is implemented with horizontal advection of hydrometeors, and redistributing snowfall across the ice sheet may lead to higher accumulation rates in regions that are very steep or regions that receive moist air from the ocean. An example is south-east Greenland, where the TAS stations are located. All stations here show an underestimated netSW by RACMO2.4p1 (Fig. 4.1), while the netLW is not underestimated in the same months, pointing to problems with snowfall (instead of, for example, summer cloud cover) that have been found in van Dalum et al. (2024) as well. However, note that van Dalum et al. (2024) used the 11 km ice-mask, while in this study the higher resolution 5.5 km ice-mask was employed, therefore snowfall (and other variables) would be expected to be better captured; while it is not possible to directly compare the modeled precipitation with observations, it is still possible to see that the SWd bias is lower here than in RACMO2.4p1-11km, where the bias was -0.6 W/m^2, and also for the SWu, where the bias was -4.5 W/m^2 (Table 4.1), (van Dalum et al., 2024). A deeper region-specific comparison of the two would be interesting in assessing RACMO2.4p1's performance in relation to its spatial resolution.

Cloud Cover

LWd is underestimated by RACMO2.4p1, especially for the lower LWd values, which are found in clear sky, thin clouds or low temperature conditions. These biases likely contribute to the year-round underestimation of netLW radiation observed across the studied AWSs (Fig. 3.3). The LWd is influenced by air temperature and cloud properties, with small biases in air temperature leading to amplified LWd errors due to non-linear relationship. However, upper air temperatures are constrained by ERA5 reanalysis, minimizing temperature-driven bias, and van Dalum et al. (2024) attributes the LWd bias mostly to cloud cover, which would be especially true under cloudy conditions, for which the LWd is heavily dependant on cloud base temperature and emissivity. SWd in overestimated by the model, which along with the underestimation of LWd could stem from an under-representation of cloud cover or clouds' optical thickness, especially for colder and drier regions. While RACMO2.4p1 incor-

porates improvements to the clouds' scheme including the explicit representation of mixed-phase clouds, uncertainties in liquid-to-ice ratio, droplet size distribution, and cloud optical properties could still be present. These biases affect both the transmissivity of SW radiation (SWd) and the emissivity of LW radiation (LWd). In addition, the netLW is constantly underestimated in RACMO2.4p1, with values more negative than observed. Therefore, a surface radiative cooling is also causing a higher vertical temperature gradient that enhances the modeled SHF, which is typically overestimated when the netLW is underestimated, like during winter at S6, S9 or KAN_M and KAN_U. This compensating effect between netLW and SHF was also present in previous versions of the model (RACMO2.3p2-2.3p3) (van Dalum et al., 2021), which then leads to accurate values for the modeled melt energy.

Roughness Lengths, Wind, Temperature and Humidity

As observed, the SHF is underestimated and the LHF is overestimated by RACMO2.4p1, on average, with the difference between observed and modeled SHF being higher during winter and at the lower stations, where ablation is higher. These stations are located in regions where the surface roughness varies strongly (Noël et al., 2018) and fixed roughness length values for heat and momentum in RACMO2.4p1 (which on glaciated tiles has not changed from the previous versions) can easily lead to biases, with the momentum roughness length being 5 mm for bare ice and 1 mm for snow-covered grid points, that indeed underestimates the observed surface roughness for momentum, especially in summer when the hummocky and rough surfaces are exposed reaching values up to 50 mm (Noël et al., 2018.) Other issues could be found in the near-surface meteorology; however, as mentioned, biases in 2 m temperature, 2 m specific humidity and 10 m wind speed are too small to explain the spread in SHF and LHF, and problems in the representation of the turbulent heat fluxes could then be related to vertical gradients of temperature, wind speed and specific humidity, which can be caused by how evaporation rates or sublimation over ice/snow are modeled and with the representation of winds (van Dalum et al., 2024). Lower stations like S5 and KAN_L show a SHF that is underestimated by RACMO2.4p1, which could be due to the proximity of S5 and KAN_L to ice-free tundra and the higher summer temperatures that impose a strong temperature gradient and S/N barrier winds (van den Broeke and Gallée, 1996), allowing for a higher turbulent exchange of heat that is difficult to portray in the model. In addition, the tile fraction of S5 is almost 1 and therefore a feedback in heat fluxes coming from the ice-free tundra is not plausible, because the SHF would then be overestimated instead of underestimated. Similarly, katabatic winds

in winter also increase the SHF - even though the temperature gradient induced barrier winds are not present - causing another peak visible at S5 and KAN_L in February (Huai et al., 2020a) that is also underestimated by RACMO2.4p1, again showing issues with how winds are modeled.

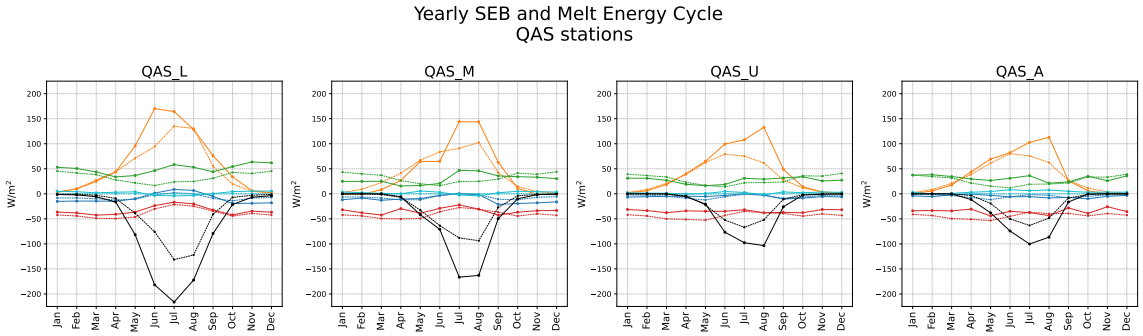

(a)

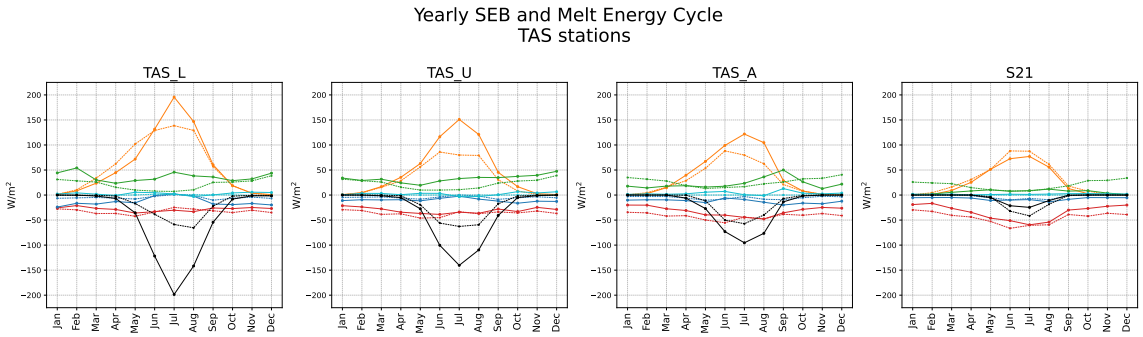

(b)

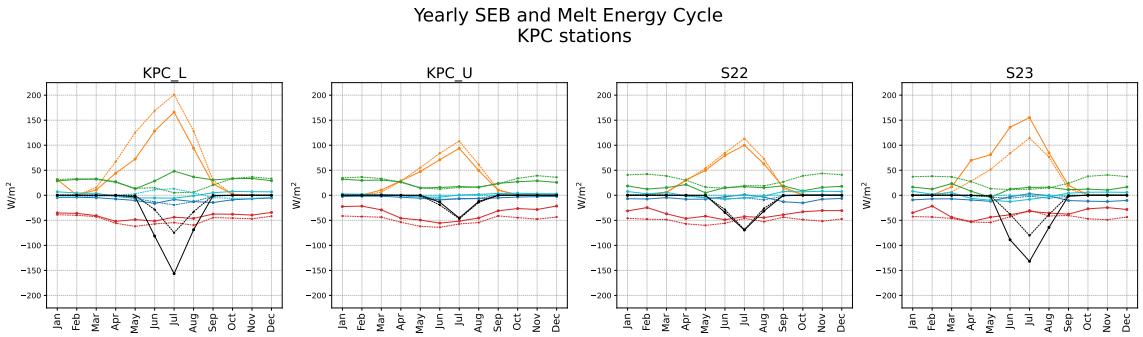

(c)

Figure 4.1: Annual cycle of energy fluxes at QAS (a), TAS (b) and KPC-S22-S23 (c) stations. The presented values are mean motnhly-means averaged through the available years of observations. The solid colored lines are observed means and the dashed lines are modeled values by RACMO2.4p1.

4.1.1 SMB

SEB biases have an impact in the annual AWSs SMB as well, which seems to be overestimated by RACMO2.4p1, especially in AWSs located closer to the ice-sheet margin. The fluxes that may cause the underestimated melt energy are, as mentioned, the net short-wave radiation, due to the overestimation of surface albedo, and the SHF, which is most likely caused by a plurality of factors. In addition to melt energy being too small, snowfall also seems to be overestimated: this in itself can explain the underestimation of melt energy, since the energy that would be available for ice-melt is used to melt the present snow, which for most of the low-lying stations is visible in the mean-monthly means plots, such as in Fig. 3.3 for S5 and KAN_L, but also TAS_L, TAS_U, QAS_L, QAS_U and KPC_L and S23 (Fig. 4.1c). Both the melt underestimation and the overestimation of snowfall lead to an overestimation by RACMO2.4p1 of the SMB, shown in the results for all AWSs and then specifically for the K-Transect (Fig. 3.5b). The same pattern is visible along the Q-Transect, where annual modeled SMB is less negative than observed, and for which the greatest difference is found at the lowest station, QAS_L, for which also the difference in melt is greater (Fig. 4.2). Stations like S6, KAN_M, S9, KPC_U are very well represented in their annual SMB, as shown in Figure 3.4, and other stations are close to the 1:1 line; difficult stations remain the QAS and the TAS, which also showed most of the problems discussed about snowfall, albedo and net short-wave radiation. All things considered, RACMO2.4p1 manages to model SMB and melt reasonably well, with improvements from its previous versions, and is a valuable tool to study the current state and evolution of the GrIS integrated SMB.

(a)

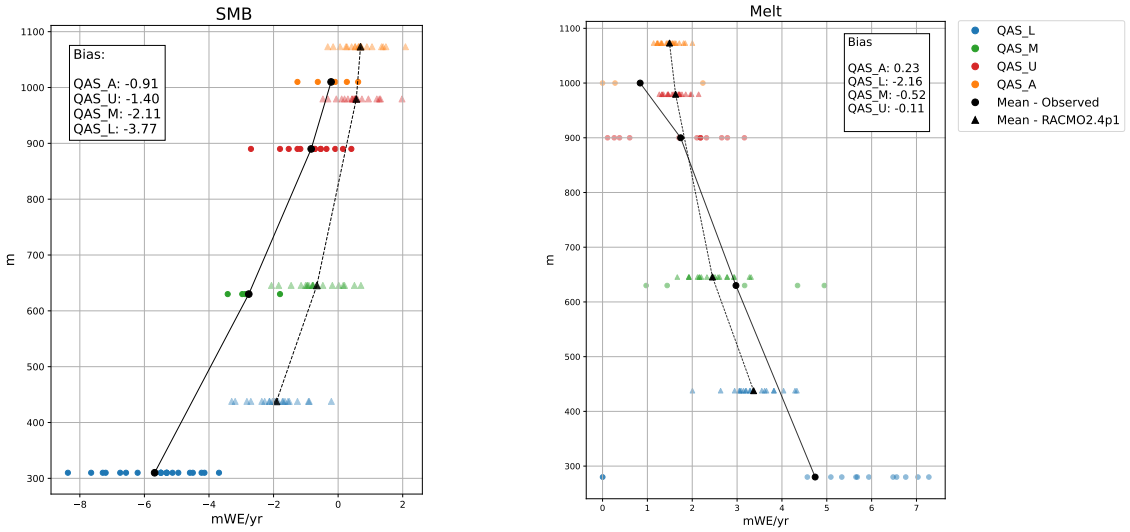

(b) (c)

Figure 4.2: Observed and RACMO2.4p1 yearly SMB and melt values for QAS_L, QAS_M, QAS_U and QAS_A. Time evolution of the yearly SMB (a); modeled and observed yearly and mean SMB for the different stations against their modeled and observed elevations (b); same as b) but for yearly melt. The bias represents the difference in the mean modeled and observed melt averaged over all available years for that station.

4.2 Integrated SMB Variability and GBI Melt connections

4.2.1 SMB: annual and spatial variability

GrIS integrated annual SMB and SMB components show strong interannual variability, as presented in Figure 3.6, and RACMO2.4p1 also shows the extreme melt events of 2012 and 2019 (Tedesco and Fettweis, 2020). The highest decrease of SMB is observed from the 1908s-1990s, mostly attributed to an increase in runoff and surface melt, since accumulation has remained basically constant (also found in other studies, Slater et al., 2021). Maps of the difference from the early and recent period (see Methods) show that SMB decreased in the ice-sheet margins widening the ablation areas, while it slightly increased in the interior parts of the ice-sheet. As a results, SMB gradients are steepened (Slater et al., 2021) and the change in SMB is reflected in the change of the other SMB components as well. Melt increased mostly everywhere (apart from in the innermost regions), but it has been buffered by the refreezing of the water percolating in the snow/ice column, for which it is possible to see that refreezing increased all around the ice sheet at the higher elevation down until the ELA, after which its buffering action decreased - since at lower elevation in the ablation zone, temperatures are not low enough to permit the refreezing of meltwater within the ice column and pore space is not sufficient. Melt water then converts into surface runoff in the ablation areas, where runoff increased strongly, especially in the west and south of the GrIS. Precipitation increased in the north-east GrIS and decreased in the south-east part, probably explaining the SMB increase in this region.

4.2.2 Connections with GBI

The large variability of melt and SMB can eb attributed tolarge scale atmospheric circulation and local feedback processes (Slater et al., 2021). Annual SMB decreases when summer GBI increases and summer melt is directly related to summer GBI, strongly increasing when the index increases. Therefore, it is melt anomalies that drive changes in the annual SMB (Hofer et al., 2017) more than precipitation changes, with R=-0.75 (Fig. 3.9). The correlation maps (Fig. 3.10a and 3.10) show the spatial response of the SMB and the SMB components to summer GBI, while the correlation maps of the SEB variables (Fig. 3.11a and 3.11) explain the higher/lower summer melt in the different regions of the GrIS. Taking as example two main regions, the SW ablation zone and the NE part of the GrIS, we can say

for the first one that higher summer GBI values cause an increase of surface melt (buffered by water retention and refreezing above the ELA) and runoff, reducing the annual SMB. For the second region, on the other hand, the SMB weakly increases when summer GBI increases, which is led by a slightly positive correlation between precipitation and JJA GBI. Zooming in and looking at the correlation for the SEB variables, it is possible to see that when JJA GBI increases, the SWd of the SW ablation zone decreases with a consequent increase of netSW. On the contrary, netSW decreases in the NE part of the GrIS, along with an increase in the netLW. The different responses of the radiative fluxes to JJA GBI increase can be due to cloud cover and/or surface albedo changes. Other studies have found that cloud cover has decreased in the past decades, especially in SW Greenland (Hofer et al., 2017), where warm air is advected from SW. On the contrary, cloud cover slightly increased in the NE part of the GrIS, where the anticyclonic conditions induced by blocking events drive moister air enhancing cloud formation. This cloud pattern explains the decrease in SWd observed in northern Greenland when the GBI increases, since a higher cloud cover (or thicker clouds) would reflect less incoming short-wave radiation. The increase in cloud cover also explains the positive sensitivity and correlation of LWd in northern Greenland, through the warming radiative effect of clouds. On the other end, less cloud cover leads to an increase of SWd in southern Greenland and a decrease in LWd. However, looking at the sensitivity maps of SWd and LWd, the first only slightly increases in SW Greenland and the latter almost does not change over summer. Therefore, SMB changes in SW Greenland are mostly driven by changes in albedo, which is what we can see in the sensitivity map of the SWu to JJA GBI: SWu strongly decreases in the western ablation region of Greenland, causing the netSW to increase in the same regions, and also overall in the margins of the ice-sheet. This albedo decrease/netSW increase is caused by the melt-albedo feedback, which is an important local feedback process impacting the annual SMB of the GrIS. When air temperature increases - i.e. warm air advection during blocking events - and melt occurs, the surface albedo decreases, leading to a higher absorption of short-wave radiation which then amplifies the temperature increase and melting itself. Another cause that can trigger the melt-albedo feedback, is if albedo shows lower values than average when summer snowfall decreases, which usually happens in SW Greenland because high pressure conditions suppress precipitation (also visible in the precipitation map in Fig. 3.10). Therefore, the increase in netSW can be due to both processes: the reduced cloud cover, that makes SWd increase, and the lower albedo, which decreases SWu (Hofer et al., 2017).

However, atmospheric circulation imposing differences in cloud cover, pressure

systems, high GBI in summer etc., are also directly affected by changes in temperature. Therefore, it would be interesting to disentangle for further research the effect on the GrIS SMB and SEB variables from temperature changes and circulation changes to clearly find the drivers and improve SMB quantification in a changing climate. In fact, atmospheric drivers are more difficult to model, and model ensembles (CMIP5 but also CMIP6) struggle to represent the observed increase in JJA GBI values in the last decades, either pointing at an internal variability as cause to this increase or at their lacking ability of representing the dynamical and physical processes causing blocking events (Delhasse et al., 2018; Delhasse et al., 2021; Tedesco and Fettweis, 2020). This would mean that the modeled future SMB decrease of the GrIS is underestimated by climate models, and considering that the impact of blockings on the SMB can double the surface mass loss so far projected (Maddison et al., 2024; Michel et al., 2021) it is relevant to study how atmospheric circulation is actually impacting the GrIS SMB and how it will change in the future.

Conclusions

In this study, data from the latest version of the regional climate model RACMO2.4p1 was employed to (1) evaluate its performance using in situ AWSs observations; (2) reconstruct the SMB of the GrIS and (3) find correlations between the SMB interannual variability and atmospheric circulation, quantified using the GBI index.

For the first research question, we find that RACMO2.4p1 realistically models near-surface meteorology and radiative fluxes while it poorly represents turbulent fluxes. At the lower stations, i.e., KAN_L, S5, QAS_L, the model slightly underestimates the netSW due to the underestimation of the surface albedo, most probably caused by too much modeled snowfall precipitation or too little snow melt. As a consequence, we find a delay in the onset of the ice ablation season, which leads to an underestimation of melt and an overestimation of SMB at different AWSs. Therefore, improvements can be made regarding the albedo and netSW representation, as well as the turbulent heat fluxes. However, the SMB is on average well represented by RACMO2.4p1, with a mean difference with in situ observations of only 1 m w.e.

RACMO2.4p1 data is therefore used to reconstruct the integrated SMB and SMB components of the GrIS from 1945 to 2023. The results show a high interannual variability and an increased declining trend of SMB from the climatological periods starting in 1982. This is attributable to the increase in surface melt and runoff, while accumulation did not decrease.

Regression analysis revealed an anti-correlation between annual SMB and summer GBI (R^2 = -0.67) which is mainly driven by the correlation between summer GBI and summer melt (R^2 = 0.85). The spatial response of summer melt to summer GBI varies regionally within the GrIS. In the SW part, high summer GBI decreases cloud cover which induces snowfall suppression. Therefore we observe a decrease in SWu and an increases in netSW, which is caused by lower surface albedo values. In the NW part of Greenland, for high summer GBI we find a netSW decrease and netLW increase, probably associated to the higher cloud cover caused by moist

air inflow caused by Greenland atmospheric blockings. Finally, we find that a one-standard-deviation increase in summer GBI results in a 102 Gt/year SMB decline, highlighting the influence of atmospheric circulation on the surface mass loss of the GrIS through increased summer melt. For further research, given the observed high anti-correlation between annual SMB and summer GBI, it would be interesting to use JJA GBI as a predictor of future annual SMB, comparing the results to what ESMs find. Also, to better constrain the current state of the GrIS SMB, improvements in RACMO2.4p1 are necessary, with an emphasis on the turbulent heat fluxes, surface albedo and precipitation.

Bibliography

Delhasse, A., Fettweis, X., Kittel, C., Amory, C., & Agosta, C. (2018). Brief communication: Impact of the recent atmospheric circulation change in summer on the future surface mass balance of the greenland ice sheet. *The Cryosphere*, *12*(11), 3409–3418. https://doi.org/10.5194/tc-12-3409-2018

Delhasse, A., Hanna, E., Kittel, C., & Fettweis, X. (2021). Brief communication: Cmip6 does not suggest any atmospheric blocking increase in summer over greenland by 2100. *International Journal of Climatology*, *41*(4), 2589–2596. https://doi.org/https://doi.org/10.1002/joc.6977

ECMWF. (2009). Ifs documentation cy33r1 - part iv: Physical processes [Operational implementation 3 June 2008]. https://doi.org/10.21957/8o7vwlbdr

ECMWF. (2020). Ifs documentation cy47r1 - part iv: Physical processes. https://doi.org/10.21957/cpmkqvhja

Fausto, R. S., van As, D., Mankoff, K. D., Vandecrux, B., Citterio, M., Ahlstrøm, A. P., Andersen, S. B., Colgan, W., Karlsson, N. B., Kjeldsen, K. K., Korsgaard, N. J., Larsen, S. H., Nielsen, S., Pedersen, A. Ø., Shields, C. L., Solgaard, A. M., & Box, J. E. (2021). Programme for monitoring of the greenland ice sheet (promice) automatic weather station data. *Earth System Science Data*, *13*(8), 3819–3845. https://doi.org/10.5194/essd-13-3819-2021

Fettweis, X. (2007). Reconstruction of the 1979ndash;2006 greenland ice sheet surface mass balance using the regional climate model mar. *The Cryosphere*, *1*(1), 21–40. https://doi.org/10.5194/tc-1-21-2007

Fettweis, X., Box, J. E., Agosta, C., Amory, C., Kittel, C., Lang, C., van As, D., Machguth, H., & Gallée, H. (2017). Reconstructions of the 1900–2015 greenland ice sheet surface mass balance using the regional climate mar model. *The Cryosphere*, *11*(2), 1015–1033. https://doi.org/10.5194/tc-11-1015-2017

Fettweis, X., Hanna, E., Lang, C., Belleflamme, A., Erpicum, M., & Gallée, H. (2013). Important role of the mid-tropospheric atmospheric circulation in the recent surface melt increase over the greenland ice sheet. *The Cryosphere*, *7*(1), 241–248. https://doi.org/10.5194/tc-7-241-2013

Hanna, E., Fettweis, X., & Hall, R. J. (2018). Brief communication: Recent changes in summer greenland blocking captured by none of the cmip5 models. *The Cryosphere*, *12*(10), 3287–3292. https://doi.org/10.5194/tc-12-3287-2018

Hanna, E., Cappelen, J., Fettweis, X., Mernild, S. H., Mote, T. L., Mottram, R., Steffen, K., Ballinger, T. J., & Hall, R. J. (2021). Greenland surface air temperature changes from 1981 to 2019 and implications for ice-sheet melt and mass-balance change. *International Journal of Climatology*, *41*(S1), E1336–E1352. https://doi.org/https://doi.org/10.1002/joc.6771

Hanna, E., Cropper, T. E., Hall, R. J., & Cappelen, J. (2016). Greenland blocking index 1851–2015: A regional climate change signal. *International Journal of Climatology*, *36*(15), 4847–4861. https://doi.org/https://doi.org/10.1002/joc.4673

Hanna, E., Cropper, T. E., Hall, R. J., Cornes, R. C., & Barriendos, M. (2022). Extended north atlantic oscillation and greenland blocking indices 1800–2020 from new meteorological reanalysis. *Atmosphere*, *13*(3). https://doi.org/10.3390/atmos13030436

Hanna, E., Hall, R. J., Cropper, T. E., Ballinger, T. J., Wake, L., Mote, T., & Cappelen, J. (2018). Greenland blocking index daily series 1851–2015: Analysis of changes in extremes and links with north atlantic and uk climate variability and change. *International Journal of Climatology*, *38*(9), 3546–3564. https://doi.org/https://doi.org/10.1002/joc.5516

Hanna, E., Huybrechts, P., Cappelen, J., Steffen, K., Bales, R. C., Burgess, E., McConnell, J. R., Peder Steffensen, J., Van den Broeke, M., Wake, L., Bigg, G., Griffiths, M., & Savas, D. (2011). Greenland ice sheet surface mass balance 1870 to 2010 based on twentieth century reanalysis, and links with global climate forcing. *Journal of Geophysical Research: Atmospheres*, *116*(D24). https://doi.org/https://doi.org/10.1029/2011JD016387

Hanna, E., Jones, J. M., Cappelen, J., Mernild, S. H., Wood, L., Steffen, K., Huybrechts, P., et al. (2013). The influence of north atlantic atmospheric and oceanic forcing effects on 1900–2010 greenland summer climate and ice melt/runoff. *Int. J. Climatol*, *33*(4), 862–880.

Hermann, M., Box, J. E., Fausto, R. S., Colgan, W. T., Langen, P. L., Mottram, R., Wuite, J., Noël, B., van den Broeke, M. R., & van As, D. (2018). Application of promice q-transect in situ accumulation and ablation measurements (2000–2017) to constrain mass balance at the southern tip of the greenland ice sheet. *Journal of Geophysical Research: Earth Surface*, *123*(6), 1235–1256. https://doi.org/https://doi.org/10.1029/2017JF004408

Hersbach, H., Bell, B., Berrisford, P., Hirahara, S., Horányi, A., Muñoz-Sabater, J., Nicolas, J., Peubey, C., Radu, R., Schepers, D., Simmons, A., Soci, C., Abdalla, S., Abellan, X., Balsamo, G., Bechtold, P., Biavati, G., Bidlot, J., Bonavita, M., … Thépaut, J.-N. (2020). The era5 global reanalysis. *Quarterly Journal of the Royal Meteorological Society*, *146*(730), 1999–2049. https://doi.org/https://doi.org/10.1002/qj.3803

Hofer, S., Tedstone, A. J., Fettweis, X., & Bamber, J. L. (2017). Decreasing cloud cover drives the recent mass loss on the greenland ice sheet. *Science Advances*, *3*(6), e1700584. https://doi.org/10.1126/sciadv.1700584

Huai, B., van den Broeke, M. R., & Reijmer, C. H. (2020a). Long-term surface energy balance of the western greenland ice sheet and the role of large-scale circulation variability. *The Cryosphere*, *14*(11), 4181–4199. https://doi.org/10.5194/tc-14-4181-2020

Huai, B., van den Broeke, M. R., & Reijmer, C. H. (2020b). Long-term surface energy balance of the western greenland ice sheet and the role of large-scale circulation variability. *The Cryosphere*, *14*(11), 4181–4199. https://doi.org/10.5194/tc-14-4181-2020

King, M. D., Howat, I. M., Candela, S. G., Noh, M. J., Jeong, S., Noël, B. P. Y., van den Broeke, M. R., Wouters, B., & Negrete, A. (2020). Dynamic ice loss from the greenland ice sheet driven by sustained glacier retreat. *Communications Earth & Environment*, *1*(1), 1. https://doi.org/10.1038/s43247-020-0001-2

Machguth, H., Thomsen, H. H., Weidick, A., Ahlstrøm, A. P., Abermann, J., Andersen, M. L., Andersen, S. B., Bjørk, A. A., Box, J. E., Braithwaite, R. J., & et al. (2016). Greenland surface mass-balance observations from the ice-sheet ablation area and local glaciers. *Journal of Glaciology*, *62*(235), 861–887. https://doi.org/10.1017/jog.2016.75

Maddison, J. W., Catto, J. L., Hanna, E., Luu, L. N., & Screen, J. A. (2024). Missing increase in summer greenland blocking in climate models. *Geophysical Research Letters*, *51*(11), e2024GL108505. https://doi.org/https://doi.org/10.1029/2024GL108505

Michel, C., Madonna, E., Spensberger, C., Li, C., & Outten, S. (2021). Dynamical drivers of greenland blocking in climate models. *Weather and Climate Dynamics*, *2*(4), 1131–1148. https://doi.org/10.5194/wcd-2-1131-2021

Morlighem, M., Williams, C., Rignot, E., An, L., Arndt, J. E., Bamber, J. L., Catania, G., Chauché, N., Dowdeswell, J. A., Dorschel, B., Fenty, I., Hogan, K., Howat, I., Hubbard, A., Jakobsson, M., Jordan, T. M., Kjeldsen, K. K., Millan, R., Mayer, L., … Weinrebe, W. (2021). Bedmachine greenland v3: A 1-km

resolution model of greenland ice sheet bed topography. *The Cryosphere*, *15*, 4487–4508. https://doi.org/10.5194/tc-15-4487-2021

Noël, B., van de Berg, W. J., van Wessem, J. M., van Meijgaard, E., van As, D., Lenaerts, J. T. M., Lhermitte, S., Kuipers Munneke, P., Smeets, C. J. P. P., van Ulft, L. H., van de Wal, R. S. W., & van den Broeke, M. R. (2018). Modelling the climate and surface mass balance of polar ice sheets using racmo2 – part 1: Greenland (1958–2016). *The Cryosphere*, *12*(3), 811–831. https://doi.org/10.5194/tc-12-811-2018

Pettersen, C., Henderson, S. A., Mattingly, K. S., Bennartz, R., & Breeden, M. L. (2022). The critical role of euro-atlantic blocking in promoting snowfall in central greenland. *Journal of Geophysical Research: Atmospheres*, *127*(6), e2021JD035776. https://doi.org/https://doi.org/10.1029/2021JD035776

Shepherd, A., Ivins, E., Rignot, E., Smith, B., van den Broeke, M., Velicogna, I., Whitehouse, P., Briggs, K., Joughin, I., Krinner, G., Nowicki, S., Payne, T., Scambos, T., Schlegel, N., A, G., Agosta, C., Ahlstrøm, A., Babonis, G., Barletta, V. R., … Team, T. I. (2020). Mass balance of the greenland ice sheet from 1992 to 2018. *Nature*, *579*(7798), 233–239. https://doi.org/10.1038/s41586-019-1855-2

Silva, T., Abermann, J., Noël, B., Shahi, S., van de Berg, W. J., & Schöner, W. (2022). The impact of climate oscillations on the surface energy budget over the greenland ice sheet in a changing climate. *The Cryosphere*, *16*(8), 3375–3391. https://doi.org/10.5194/tc-16-3375-2022

Slater, T., Shepherd, A., McMillan, M., Leeson, A., Gilbert, L., Muir, A., Munneke, P. K., Noël, B., Fettweis, X., van den Broeke, M., & Briggs, K. (2021). Increased variability in greenland ice sheet runoff from satellite observations. *Nature Communications*, *12*(1), 6069. https://doi.org/10.1038/s41467-021-26229-4

Smeets, P. C. J. P., Munneke, P. K., van As, D., van den Broeke, M. R., Boot, W., Oerlemans, H., Snellen, H., Reijmer, C. H., & van de Wal, R. S. W. (2018). The k-transect in west greenland: Automatic weather station data (1993–2016). *Arctic, Antarctic, and Alpine Research*, *50*(1), S100002. https://doi.org/10.1080/15230430.2017.1420954

Tedesco, M., & Fettweis, X. (2020). Unprecedented atmospheric conditions (1948–2019) drive the 2019 exceptional melting season over the greenland ice sheet. *The Cryosphere*, *14*(4), 1209–1223. https://doi.org/10.5194/tc-14-1209-2020

Tiggelen, M. V., Smeets, P. C. J. P., Reijmer, C. H., van As, D., Box, J. E., Fausto, R. S., Khan, S. A., Rignot, E., & van den Broeke, M. R. (2024). *Daily surface energy balance (seb) and quality-controlled meteorological quantities measured*

at 19 stations on the greenland ice sheet (2003-2023) (dataset). dataset. PANGAEA. https://doi.org/10.1594/PANGAEA.970127

Undén, P., Rontu, L., Järvinen, H., Lynch, P., Calvo-Sanchez, J., Cats, G., Cuxart, J., Eerola, K., Fortelius, C., & García-Moya, J. (2002). Hirlam-5 scientific documentation [No further details available.]. *HIRLAM Scientific Reports*.

van Dalum, C. T., van de Berg, W. J., Gadde, S. N., van Tiggelen, M., van der Drift, T., van Meijgaard, E., van Ulft, L. H., & van den Broeke, M. R. (2024). First results of the polar regional climate model racmo2.4. *The Cryosphere*, *18*(9), 4065–4088. https://doi.org/10.5194/tc-18-4065-2024

van Dalum, C. T., van de Berg, W. J., & van den Broeke, M. R. (2021). Impact of updated radiative transfer scheme in snow and ice in racmo2.3p3 on the surface mass and energy budget of the greenland ice sheet. *The Cryosphere*, *15*(4), 1823–1844. https://doi.org/10.5194/tc-15-1823-2021

van Tiggelen, M., Smeets, P. C. J. P., Reijmer, C. H., van As, D., Box, J. E., Fausto, R. S., Khan, S. A., Rignot, E., & van den Broeke, M. R. (2024a). Surface energy balance closure over melting snow and ice from in situ measurements on the greenland ice sheet. *Journal of Glaciology*, 1–11. https://doi.org/10.1017/jog.2024.68

van Tiggelen, M., Smeets, P. C. J. P., Reijmer, C. H., van As, D., Box, J. E., Fausto, R. S., Khan, S. A., Rignot, E., & van den Broeke, M. R. (2024b). Surface energy balance closure over melting snow and ice from in situ measurements on the greenland ice sheet. *Journal of Glaciology*, 1–11. https://doi.org/10.1017/jog.2024.68

van den Broeke, M. R., Enderlin, E. M., Howat, I. M., Kuipers Munneke, P., Noël, B. P. Y., van de Berg, W. J., van Meijgaard, E., & Wouters, B. (2016). On the recent contribution of the greenland ice sheet to sea level change. *The Cryosphere*, *10*(5), 1933–1946. https://doi.org/10.5194/tc-10-1933-2016

van den Broeke, M. R., Box, J., Fettweis, X., Hanna, E., Noël, B., Tedesco, M., van As, D., van de Berg, W. J., & van Kampenhout, L. (2017). Greenland ice sheet surface mass loss: Recent developments in observation and modeling. *Current Climate Change Reports*, *3*(4), 345–356. https://doi.org/10.1007/s40641-017-0084-8

van den Broeke, M. R., & Gallée, H. (1996). Observation and simulation of barrier winds at the western margin of the greenland ice sheet. *Quarterly Journal of the Royal Meteorological Society*, *122*(534), 1365–1383. https://doi.org/10.1002/qj.49712253407

Vandecrux, B., Box, J. E., Ahlstrøm, A. P., Andersen, S. B., Bayou, N., Colgan, W. T., Cullen, N. J., Fausto, R. S., Haas-Artho, D., Heilig, A., Houtz, D. A.,

How, P., Iosifescu Enescu, I., Karlsson, N. B., Kurup Buchholz, R., Mankoff, K. D., McGrath, D., Molotch, N. P., Perren, B., … Steffen, K. (2023). The historical greenland climate network (gc-net) curated and augmented level-1 dataset. *Earth System Science Data*, *15*(12), 5467–5489. https://doi.org/10.5194/essd-15-5467-2023

Ward, J. L., Flanner, M. G., & Dunn-Sigouin, E. (2020). Impacts of greenland block location on clouds and surface energy fluxes over the greenland ice sheet [e2020JD033172 2020JD033172]. *Journal of Geophysical Research: Atmospheres*, *125*(22), e2020JD033172. https://doi.org/https://doi.org/10.1029/2020JD033172